Investigation of Solidification Pathways in CoSi Alloys

Submitted By
Stan Barlow

IN PARTIAL FULFILLMENT OF THE REQUIREMENTS FOR AN UNDERGRADUATE THESIS WITH A

BACHELOR OF SCIENCE IN MECHANICAL ENGINEERING

School of Engineering
Tufts University
Medford, Massachusetts

May 2017

Signature of Author:
Stan Barlow

Certified By:
Associate Professor Douglas M. Matson
Department of Mechanical Engineering
Tufts University

Committee:
Postdoctoral Fellow Sangho Jeon
Department of Mechanical Engineering
Tufts University

Committee:
Research Assistant Professor Jonghyun Lee
Mechanical and Industrial Engineering Dept.
University of Massachusetts - Amherst

Abstract

$Co_{38.5}Si_{61.5}$ and $Co_{60}Si_{40}$ eutectic alloys were melted and solidified on an electrostatic levitator (ESL) at various undercoolings in order to determine their phase transformations along the transition from a liquid to a solid state. Investigation into the solidification velocity of constituent phases identified specific solidification pathways relative to first recalescence undercooling. Results indicated two different thermal events for both alloys. A critical undercooling of 81.5 K during the first recalescence of $Co_{38.5}Si_{61.5}$ was established, below which solidification velocity was faster during first recalescence and slower during second recalescence than were respective velocities above the temperature split. A similar critical undercooling of 50 K was found for the $Co_{60}Si_{40}$ alloy, where similar velocity relationships were observed. It is also speculated that a critical undercooling is necessary during second recalescence following high undercoolings in first recalescence in order to lower the energy required for nucleation to occur. Metallography showed that delay time between recalescence events has an effect on morphology change during solidification. The findings presented in this thesis support prior work done involving similar research with both CoSi eutectic alloys.

Acknowledgements

The author would like to thank Trudy Allen, Glenn Fountain, and Mike SanSoucie of NASA's Marshall Space Flight Center (MSFC) for technical assistance. The author would also like to thank Justin Rodriguez for providing the software used to analyze solidification velocity, Sangho Jeon for providing undercooling and delay time calculations, and Doug Matson for providing opportunity, assistance, and simple life advice. This work was funded by NASA under grant number NNX16AB59G.

Table of Contents

1		Introduction	1
2		Background	3
	2.1	Benefits of containerless processing	3
	2.2	Rapid solidification of eutectic alloys	3
	2.2	Solidification pathways of CoSi alloys	5
3		Methodology	9
	3.1	Sample preparation	9
	3.2	ESL experiments	9
4		Results	11
	4.1	Data tables	11
	4.2	Undercooling and delay time analysis techniques	18
	4.3	Velocity analysis techniques	20
5		Discussion	22
	5.1	$Co_{38.5}Si_{61.5}$ solidification pathways	22
	5.2	$Co_{60}Si_{40}$ solidification pathways	34
6		Conclusions	46
7		Future Work	47
8		References	48

List of Tables

TABLE I $Co_{38.5}Si_{61.5}$ Undercooling and Solidification Data 11
TABLE II $Co_{60}Si_{40}$ Undercooling and Solidification Data 14

List of Figures

Figure 1 Phase diagram for the CoSi system 5
Figure 2 Synchrotron x-ray graphs for phase formation in $Co_{38.5}Si_{61.5}$ 7
Figure 3 The electrostatic levitator at NASA MSFC 9
Figure 4 Internal view of the levitator and a levitated droplet 10
Figure 5 Time-temperature graph for a $Co_{60}Si_{40}$ melt cycle 18
Figure 6 Solidification velocity analysis 20
Figure 7 1^{st} high temp. vs. 1^{st} undercooling for the $Co_{38.5}Si_{61.5}$ system 23
Figure 8 1^{st} high temp. vs. 2^{st} undercooling for the $Co_{38.5}Si_{61.5}$ system 24
Figure 9 2^{nd} high temp. vs. 2^{nd} undercooling for the $Co_{38.5}Si_{61.5}$ system 25
Figure 10 2^{nd} high temp. vs. 1^{st} undercooling for the $Co_{38.5}Si_{61.5}$ system 26
Figure 11 1^{st} solid. velocity vs. 1^{st} undercooling for the $Co_{38.5}Si_{61.5}$ system 27
Figure 12 2^{nd} solid. velocity vs. 1^{st} undercooling for the $Co_{38.5}Si_{61.5}$ system 28
Figure 13 Delay time vs 1^{st} undercooling for the $Co_{38.5}Si_{61.5}$ system 29
Figure 14 Metallography of $Co_{38.5}Si_{61.5}$ regions 1, 2, and 3A and 3B 30
Figure 15 Difference in temperature profile of $Co_{38.5}Si_{61.5}$ regions 3A and 3B 31
Figure 16 Delay time vs. 2^{nd} undercooling for the $Co_{38.5}Si_{61.5}$ system 32
Figure 17 2^{nd} solid. velocity vs. 2^{st} undercooling for the $Co_{38.5}Si_{61.5}$ system 33
Figure 18 1^{st} high temp. vs. 1^{st} undercooling for the $Co_{60}Si_{40}$ system 35
Figure 19 1^{st} high temp. vs. 2^{st} undercooling for the $Co_{60}Si_{40}$ system 36
Figure 20 2^{nd} high temp. vs. 2^{nd} undercooling for the $Co_{60}Si_{40}$ system 37
Figure 21 2^{nd} high temp. vs. 1^{st} undercooling for the $Co_{60}Si_{40}$ system 38
Figure 22 1^{st} solid. velocity vs. 1^{st} undercooling for the $Co_{60}Si_{40}$ system 39
Figure 23 2^{nd} solid. velocity vs. 1^{st} undercooling for the $Co_{60}Si_{40}$ system 41
Figure 24 Delay time vs 1^{st} undercooling for the $Co_{60}Si_{40}$ system 42
Figure 25 Delay time vs. 2^{nd} undercooling for the $Co_{60}Si_{40}$ system 44
Figure 26 2^{nd} solid. velocity vs. 2^{st} undercooling for the $Co_{60}Si_{40}$ system 45

1 Introduction

Advances in material science have always paved the way for advances in technology. Much in the way that steel in the late 1800s revolutionized the construction industry and silicon in the 1970s created the modern information technology industry, discoveries of advanced materials should progress established and emerging industries alike [1]. A thorough understanding of the thermophysical properties of a new metal material and the formation of its microstructures along its solidification pathways are absolutely necessary in order to model casting and forging processes and ultimately use the material in industry [2].

The importance of the liquid phase of metals has only recently been recognized. The way a metal solidifies has an effect on the properties of the final material, so an understanding of the properties of the liquid phase and the solidification process is becoming a necessary course of study. However, the high temperatures necessary to melt a metal, combined with the complexity of the physics of fluid flow, pose a set of challenges to experimental design. The field has turned to containerless processing methods such as electrostatic levitation (ESL) and electromagnetic levitation (EML) in order to provide an uncontaminated, undisturbed testing site [2]. ESL involves levitating a sample between electrodes in a vacuum chamber while EML holds the sample suspended in a magnetic field induced by a series of coils.

The solidification of binary eutectic alloys is gathering interest in scientific communities due to the potential applications of the alloys in industry. Eutectic alloys, or mixtures of substances that melt and solidify at temperatures lower than the melting points of the separate constituents or other compositions of them, are desirable

industrial compounds due to these relatively low melting temperatures [3]. Binary eutectics also solidify in an interesting manner, as multiphase growth is often observed. The combination of different solid phases, or arrangement of atoms within a crystalline solid, can result in unique material properties. For example, a fragile yet high-strength phase deposited into a ductile matrix would result in a strong yet flexible material [2].

When a material solidifies, no matter the specific phase that forms, atoms from the liquid bond together and begin to form crystals as a result of a loss in free energy. The location of these crystals are referred to as nucleation points or nucleation sites. When samples are undercooled below their melting temperature, crystal growth, or nucleation, involves the formation of dendrites, which grow fractally through the liquid. The growth rate, or solidification velocity, of these dendrites within different phases is important to the understanding of the structures that compose the metal state [4]. Different solidification rates can correspond to a different solidification pathway, or order of phases formed, as the metal transitions from a liquid phase to a metastable solid phase and ultimately to a stable solid phase, each of which might have a different growth rate [3] [5]. Ultimately, an understanding of the solidification pathways and the conditions that determine pathway selection can allow for the production of materials with desirable overall properties, which depend on those of the material's constituent microstructures and phases.

2 Background

2.1 Benefits of containerless processing

Containerless processing provides a unique and productive method for analyzing the properties of undercooled liquid metals. Eliminating the contact between the sample and its container reduce the possibility of surface contamination and increase the level of surface nucleation control [2]. A pure, uncontaminated sample can be deeply undercooled below melting temperature before recalescence, or rapid solidification, occurs. This undercooling enables the analysis of non-equilibrium phases, structural changes in the melt, and thermophysical properties such as density, viscosity, and surface tension [6]. Electrostatic levitation [3] [7] [8] [9] [10], electromagnetic levitation [3] [8] [11], and drop tubes [5] [12] have all previously been used to investigate the solidification of molten metals.

2.2 Rapid solidification of eutectic alloys

The rapid solidification of metals allows the formation of refined microstructures and metastable phases, which can have useful applications as previously discussed. Rapid solidification of eutectic compositions results in finer microstructures developed than in their non-eutectic counterparts, which further improve their mechanical properties [5]. There are three primary eutectic reactions for binary alloys: solid solution-solid solution (ss-ss) eutectics, solid solution-intermetallic compound (ss-ic) eutectics, and intermetallic compound-intermetallic compound (ic-ic) eutectics. Each reaction results in differing growth rates and phase and microstructure formations [8].

Regular eutectic structures involve lamellar and rod structures. Lamellar structures are composed of fine layered plates of alternating materials. They are typically rectangular over long distances. Rods are similarly layered plates but are polygonal rather than rectangular. Anomalous eutectics label the formation of lamellar and rod structures interspersed with irregularities such as broken or branched plates, blobs, or fibrous arrays [13] [14]. It has long been observed that the solidification of a metallic eutectic involves phase transitions from regular to a mix of regular and anomalous to fully anomalous eutectic microstructures [8], and it has been suggested that the formation of the anomalous eutectic is related to the crystallographic formation of the terminal eutectic phases in ss-ic alloys [11]. Anomalous eutectic formation has been observed to take place when the primary solid, or the first phase to solidify, of an ss-ss or ss-ic eutectic remelts during recalescence [15] [16] [17] [18].

A study by X. X. Wei et. al. [15] found that during the rapid solidification of ss-based undercooled eutectic, the primary solid to form will be partially remelted due to supersaturation with solute. The deeper the undercooling, the more the phase remelts upon recalescence. The remelted fraction of the solid solution then shifts the composition of the liquid away from the eutectic, resulting in the formation of anomalous compounds. However, no remelting was observed within the intermetallic compound eutectics, and thus no anomalous structures were present in ic-ic eutectics. In an attempt to better understand the solidification pathways of such ic-ic systems, cobalt-silicon (CoSi) was studied at two of its eutectic points.

2.3 Solidification pathways of CoSi alloys

The two alloys studied in this thesis were $Co_{38.5}Si_{61.5}$ and $Co_{60}Si_{40}$. These alloys are very close to two eutectic points within the system, labeled by red points in Figure 1 below. Two recalescence events are often observed during cooling at each eutectic point, as each alloy first transitions from a liquid to a metastable solid phase and then to a stable solid phase.

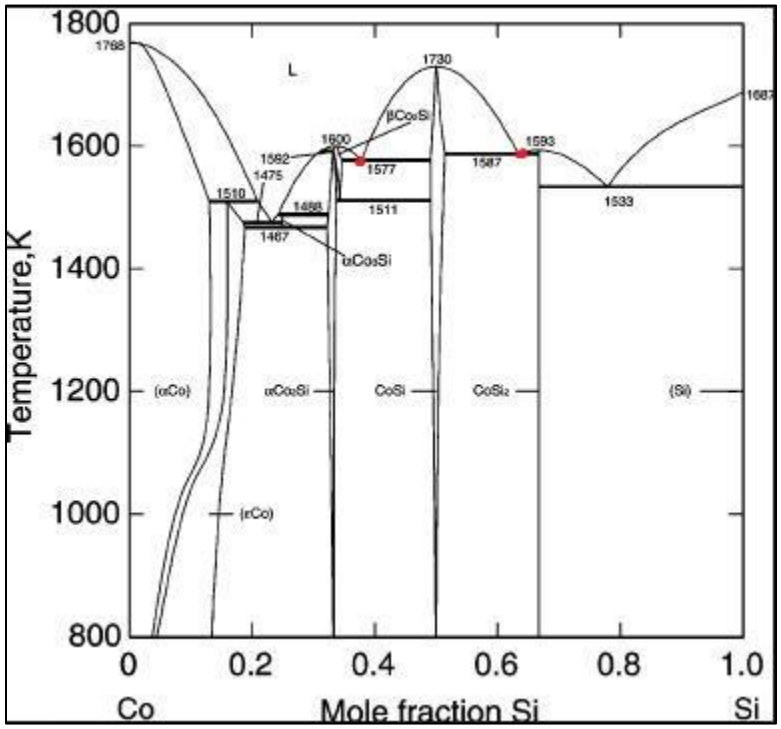

Figure 1: Phase diagram for the CoSi system

At 40% atomic Si two solid phases can form, either the metastable α-Co_2Si and CoSi or the stable β-Co_2Si and CoSi [7]. At the 61.5% atomic Si, the two phases that can form are CoSi and $CoSi_2$ [3]. The microstructural evolution of these phases for each alloy have been studied in several different publications [3] [5] [7] [8] [12], and this thesis serves to compare those results to results acquired using different methods.

A publication by W. J. Yao et. al. [5] involved testing the two above eutectics in a drop tube. Their findings characterized the microstructures of the $Co_{38.5}Si_{61.5}$ eutectic as lamellar and anomalous eutectic structures of $CoSi_2$ and CoSi phases. Smaller droplets contained more anomalous eutectic volume fraction than larger ones. The $Co_{60}Si_{40}$ eutectic displayed lamellar and anomalous eutectic structures of the CoSi and Co_2Si phases. Again, decreasing droplet size increased the relative amount of anomalous eutectic. The authors concluded that the primary nucleation phase is the $CoSi_2$ compound for the $Co_{38.5}Si_{61.5}$ eutectic and CoSi for the $Co_{60}Si_{40}$ eutectic. W. J. Yao was involved in another publication [12] that reached the same conclusions for the $Co_{60}Si_{40}$ system.

Results from a manuscript by Y. Wang, et. al. [7] using ESL to study $Co_{60}Si_{40}$ indicate that longer delay times between recalescence events promote the growth of the α-Co_2Si and CoSi eutectic phases, leaving less liquid available during the second recalescence event. The formation of phases shifts the apparent composition of the remaining liquid left or right depending on which of the two phases forms first. The solidification velocities of the recalescence events were studied to attempt to find a relationship between phase formation and undercooling. It was concluded that the alloy had three different solidification pathways. At low undercoolings, the CoSi phase crystallized as the primary solid. At medium (50 – 90 K) undercoolings, the dendrite formation of CoSi was suppressed, allowing the stable β-Co_2Si/CoSi eutectic to crystallize as the primary solid. At high (>90 K) undercoolings, the dendrite formation of CoSi was again suppressed, but the metastable α-Co_2Si/CoSi eutectic crystallized as the primary solid. These findings support the work done by W. J. Yao et. al. [5] above.

A separate paper written by Y. K. Zhang et. al. [3] focused on $Co_{38.5}Si_{61.5}$. It found a similar undercooling cutoff, on either side of which a different solidification pathway was followed. Under an undercooling of 88 K, CoSi formed the primary solid. Above it, $CoSi_2$ crystallized first. This work is supported by similar conclusions from M. Li et. al. [8], who used x-ray diffraction in ESL and EML to identify the solidification pathways of $Co_{38.5}Si_{61.5}$. The cutoff undercooling they found was 75 K. Both Zhang and Wang found that CoSi has a higher growth velocity than does $CoSi_2$.

Another method of analyzing the solidification pathway is to use x-ray data gathered from a synchrotron. Using x-ray diffraction in combination with EML, the formation of different microstructures can be identified with respect to time based on spectrometry [19].

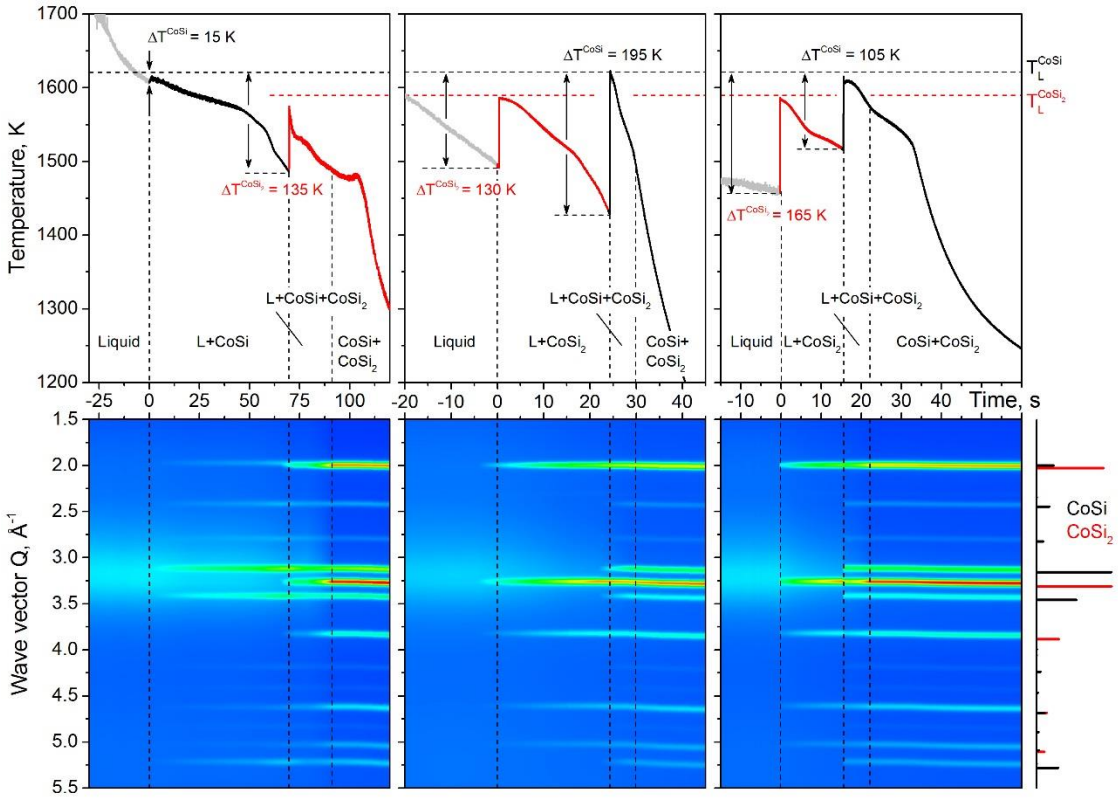

Figure 2: Synchrotron x-ray graphs for the phase formation in $Co_{38.5}Si_{61.5}$ [20]

Preliminary results in understanding the order of phase formation of $Co_{38.5}Si_{61.5}$ display a relationship between the undercooling of the first recalescence event and the first phase to form. Given large first-recalescence undercoolings, the $CoSi_2$ phase forms first – notice the red-marked wave vectors indicating the presence of $CoSi_2$ appearing before the black-marked ones in the middle and right graphs in Figure 2 above. The relative reduction in available liquid silicon pushes the composition left on the phase diagram, and eventually CoSi begins to precipitate, pushing the composition back towards the right. However, at a lower first recalescence undercooling, such as in the left-most panel of Figure 2, CoSi precipitates first. These initial findings support the work of Zhang et. al. discussed above.

3 Methodology

3.1 Sample preparation

Twenty-five samples each of both $Co_{60}Si_{40}$ and $Co_{38.5}Si_{61.5}$ were prepared by arc-melting 99.99% pure elemental Co and Si in a gettered argon atmosphere. The average error in atomic percent from desired was kept under 1%. The masses ranged from 26.597 mg to 39.927 mg, with mass losses during experimentation averaging 0.53% of the post-test mass.

3.2 ESL experiments

The electrostatic levitation (ESL) experiments were conducted at a facility at Marshall Space Flight Center (MSFC) in Huntsville, AL. The technique levitates the sample between two oppositely-charged electrodes. Positioning lasers and a feedback loop ensure the stability of the sample. The chamber is pumped to a near-vacuum to prevent arcing between the electrodes and to ensure the containerless processing of the sample.

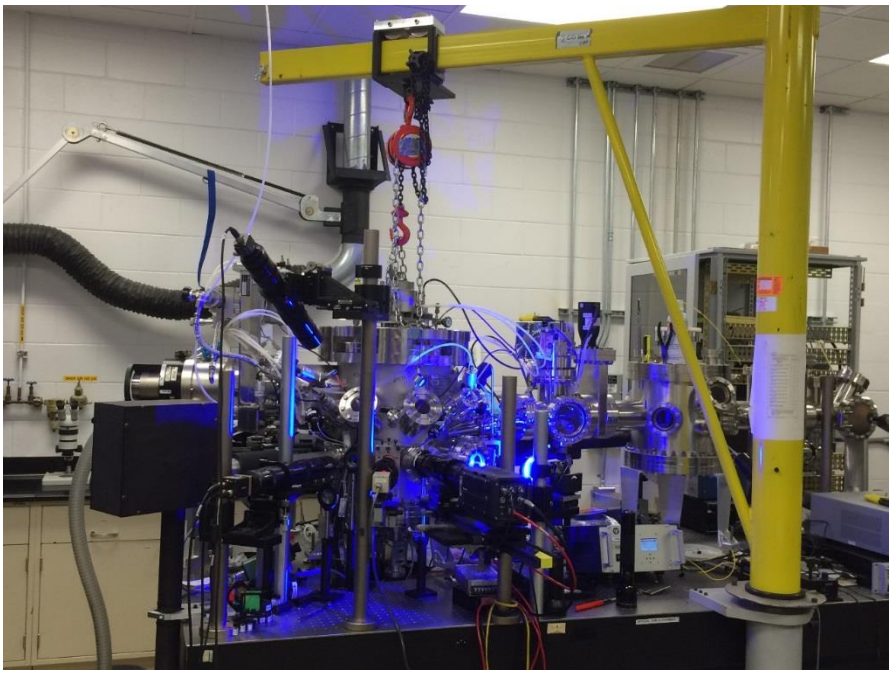

Figure 3: The electrostatic levitator at NASA MSFC

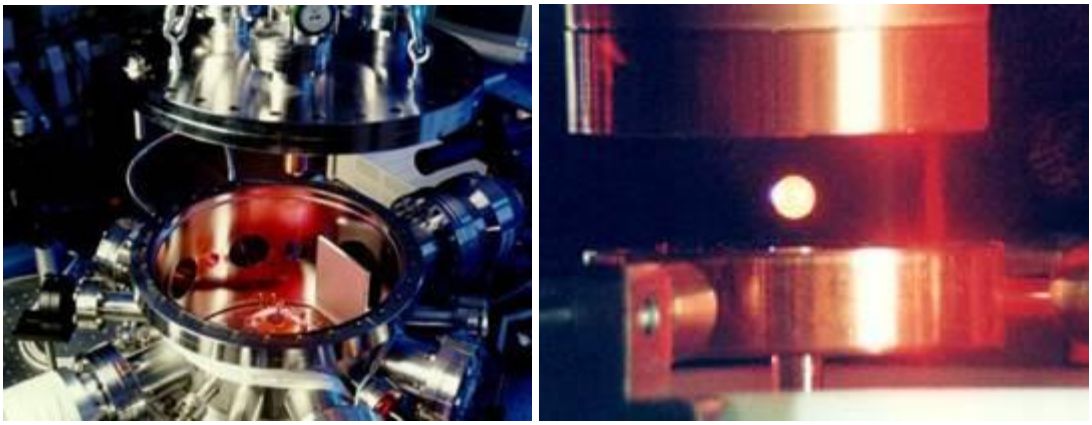

Figure 4: The inside of the MSFC ESL (L) and a molten levitated droplet (R). Photos courtesy of NASA/MSFC ESL staff.

Upon the stability of the sample, a heating laser was used to melt or hold the sample within a desired temperature range. In each melt cycle, the sample was superheated to burn off any surface oxides and impurities. The laser was switched off, and the sample was allowed to cool to solidification. Recalescence events were captured by two high-speed video cameras recording at 10,000 fps. The surface temperature of the sample was measured by a pyrometer.

4 Results

4.1 Data tables

TABLE I: $Co_{38.5}Si_{61.5}$ Undercooling and Solidification Data

Sample	Melt Cycle	Recalescence	Undercooling (K)	Velocity (m/s)	Delay Time (s)
MAT-1000	1	1		0.0874	5.000
		2	49.94		
MAT-1000	2	1	54.16		
		2			
MAT-1000	3	1	16.92	0.199	4.800
		2	43.93	0.103	
MAT-1001	2	1			6.240
		2	63.87	0.165	
MAT-1001	3	1	59.42	0.255	
		2			
MAT-1007	1	1	5.000		6.600
		2		0.290	
MAT-1007	2	1	67.84	0.176	6.640
		2	26.96	0.248	
MAT-1007	3	1	90.73	0.164	11.76
		2	90.05	4.00	
MAT-1007	4	1	89.70	0.255	12.35
		2	114.6	2.66	
MAT-1007	5	1	102.4		11.78
		2	111.4		
MAT-1007	6	1	93.20		11.85
		2	126.1		
MAT-1007	7	1	94.13		11.84
		2	112.3		
MAT-1007	8	1	95.96		11.96
		2	117.9		
MAT-1007	9	1	98.74		11.78
		2	121.5		
MAT-1007	10	1	100.6		11.52
		2	118.8		
MAT-1007	11	1	108.9		11.34
		2	118.7		
MAT-1007	12	1	97.83		11.54
		2	151.0		
MAT-1007	13	1	130.3		10.63
		2	112.3		

MAT-1007	14	1	172.0		9.634
		2	137.2		
MAT-1007	15	1	149.8		9.935
		2	128.8		
MAT-1007	16	1	198.1		8.810
		2			
MAT-1008	1	1	67.42	0.227	11.80
		2	108.4	0.360	
MAT-1009	1	1	38.89		5.400
		2	71.87	0.998	
MAT-1009	2	1	56.36	1.16	5.100
		2	76.88	0.430	
MAT-1009	3	1	66.91	0.224	11.28
		2	106.1	2.56	
MAT-1010	1	1	76.83	0.206	11.50
		2		1.54	
MAT-1010	2	1	88.65	0.319	11.40
		2		2.36	
MAT-1010	3	1	69.85	0.203	11.00
		2	101.1		
MAT-1010	4	1	55.41		11.40
		2	147.9		
MAT-1010	5	1	76.35		11.60
		2	123.3		
MAT-1010	6	1	87.29		5.700
		2	29.92		
MAT-1010	7	1	62.68		11.20
		2	162.1		
MAT-1010	8	1	80.90		12.10
		2	128.7		
MAT-1010	9	1	90.02		11.62
		2	115.1		
MAT-1010	10	1	97.32		11.57
		2	126.0		
MAT-1010	11	1	105.6		11.46
		2	126.1		
MAT-1010	12	1	144.8		10.41
		2	117.9		
MAT-1010	13	1	106.5		11.22
		2	118.8		
MAT-1010	14	1	125.6		11.05
		2	123.3		
MAT-1010	15	1	158.6		9.800
		2	120.6		

MAT-1013	1	1	25.45		7.000
		2	70.85	0.123	
MAT-1013	2	1	12.82		6.660
		2	70.86	0.189	
MAT-1013	3	1	20.10		6.300
		2	62.82	0.162	
MAT-1014	1	1	82.60	0.211	12.18
		2	87.16	3.32	
MAT-1014	2	1	72.84	0.245	12.35
		2	64.34	1.91	
MAT-1014	3	1	92.31	0.315	12.11
		2	103.2	2.11	
MAT-1015	1	1	60.96	0.135	9.800
		2	153.2	1.92	
MAT-1015	2	1	61.36		1.020
		2	26.98		
MAT-1016	1	1	35.20		12.00
		2	104.3		
MAT-1016	2	1	67.12		
		2			
MAT-1016	3	1	52.14	0.167	11.60
		2	164.1	2.80	
MAT-1017	1	1	70.08	0.277	9.300
		2	78.86		
MAT-1017	2	1	76.99		10.62
		2	168.7	1.67	
MAT-1019	1	1	70.16		11.10
		2	103.9	1.49	
MAT-1019	2	1	69.80	0.163	10.94
		2	92.78	2.28	
MAT-1019	3	1	15.46		6.080
		2	64.87	0.223	
MAT-1019	4	1			6.300
		2	62.88		
MAT-1021	1	1	72.00	0.314	3.700
		2	17.99		
MAT-1021	2	1	62.49	0.151	11.52
		2	108.4	0.994	
MAT-1045	1	1	59.72	0.175	3.000
		2	14.99		
MAT-1045	2	1	61.12	0.168	6.060
		2	28.97	0.121	
MAT-1045	3	1	59.80	0.181	11.06
		2	72.12	2.02	

MAT-1047	1	1	66.36		0.4000
		2	12.99		
MAT-1047	2	1	63.99	0.226	2.460
		2	17.99		
MAT-1047	3	1	84.64	0.184	10.73
		2	85.66	1.35	

Table I above provides the sample name, melt cycle, and delay time between recalescence events for the $Co_{38.5}Si_{61.5}$ alloy. It also displays the calculated undercooling and solidification velocities for each respective recalescence event. Blank cells indicate a lack of data or an omission of bad data. Red velocity values indicate nucleation on the back surface of the sample.

TABLE II: $Co_{60}Si_{40}$ Undercooling and Solidification Data

Sample	Melt Cycle	Recalescence	Undercooling (K)	Velocity (m/s)	Delay Time (s)
MAT-1004	1	1			7.100
		2	148.3	0.917	
MAT-1004	2	1	12.99		7.000
		2	143.3	0.979	
MAT-1006	1	1	3.000		8.000
		2	140.8	1.25	
MAT-1006	2	1			8.460
		2	131.5	1.06	
MAT-1006	3	1			8.700
		2	141.4	2.12	
MAT-1022	1	1	11.00		8.400
		2	140.5		
MAT-1022	2	1	16.99		7.700
		2	114.5	1.56	
MAT-1022	3	1	24.98		7.500
		2	117.5	0.940	
MAT-1022	4	1	55.89	0.180	6.360
		2	131.4	1.09	
MAT-1023	1	1	20.66	0.301	8.144
		2	153.3	0.779	
MAT-1023	2	1	44.28	0.119	7.628
		2	156.8	1.09	

MAT-1023	3	1	40.94	0.128	7.533
		2	156.8	1.06	
MAT-1024	1	1	46.71	0.173	5.887
		2	148.5	0.948	
MAT-1024	2	1	54.17	0.180	5.625
		2	145.6	0.993	
MAT-1024	3	1	16.44		6.367
		2	162.5		
MAT-1025	1	1	33.31	0.254	7.075
		2	171.7		
MAT-1025	2	1	41.04	0.0382	6.972
		2	153.0	1.01	
MAT-1025	3	1	32.36	0.0867	7.092
		2	156.2	1.23	
MAT-1026	1	1	19.06	0.153	8.587
		2	167.6	1.64	
MAT-1026	2	1	33.99	0.240	8.009
		2	175.7	0.711	
MAT-1026	3	1	39.74	0.0494	7.639
		2	158.7	0.568	
MAT-1027	1	1	57.78	0.0361	
		2			
MAT-1028	1	1	6.637	0.317	8.784
		2	182.7	1.70	
MAT-1028	2	1	171.6	2.28	3.410
		2	200.0		
MAT-1029	1	1	44.16	0.0682	7.016
		2	161.5	1.17	
MAT-1029	2	1	34.71	0.0944	7.191
		2	157.5		
MAT-1029	3	1	50.91	0.126	6.029
		2	150.0	0.828	
MAT-1031	1	1	10.78		7.938
		2	152.8	0.377	
MAT-1031	2	1	26.19	0.276	7.078
		2	154.5	0.814	
MAT-1031	3	1	19.23	0.166	6.957
		2	150.5		
MAT-1032	1	1	3.999		8
		2	108.5	1.15	
MAT-1032	2	1	4.999		7.9
		2	107.6	1.23	
MAT-1032	3	1			8.1
		2	128.4	0.928	

MAT-1033	1	1	109.9	0.964	3.616
		2	163.2	1.30	
MAT-1033	2	1	55.13	0.131	5.692
		2	154.7	0.940	
MAT-1033	3	1	6.562		7.120
		2	145.8	0.831	
MAT-1033	4	1		2.32	
		2	293.8	2.76	
MAT-1034	1	1	61.86		6.900
		2	109.6	0.996	
MAT-1034	2	1	19.99		7.380
		2	111.6	1.04	
MAT-1034	3	1	29.97		7.080
		2	109.6	0.942	
MAT-1034	4	1	15.23		7.380
		2	101.4		
MAT-1034	5	1	12.55		7.260
		2	92.45		
MAT-1034	6	1	82.35		12.90
		2	196.1		
MAT-1034	7	1	10.76		7.200
		2	96.05		
MAT-1034	8	1	53.86		1.900
		2	68.92		
MAT-1034	9	1	31.40		6.600
		2	89.77		
MAT-1034	10	1	66.52		5.300
		2	88.01		
MAT-1034	11	1	46.72		5.900
		2	100.6		
MAT-1034	12	1	59.32		5.500
		2	97.04		
MAT-1034	13	1	46.74		5.700
		2	97.00		
MAT-1034	14	1	14.36		6.600
		2	90.77		
MAT-1034	15	1	13.46		6.300
		2	83.60		
MAT-1035	1	1	8.390		6.471
		2	163.2	1.62	
MAT-1035	2	1	7.802		6.625
		2	154.7	0.962	
MAT-1035	3	1	16.54	0.271	5.224
		2	145.8	0.679	

MAT-1035	4	1			
		2	293.8	2.42	
MAT-1036	1	1	14.63	0.125	8.425
		2	158.0	0.812	
MAT-1036	2	1	16.96	0.149	8.528
		2	160.7	1.04	
MAT-1036	3	1	16.15	0.399	2.114
		2	82.74	0.117	
MAT-1037	1	1	5.999		6.400
		2	107.6	0.608	
MAT-1037	2	1	16.99		6.300
		2	104.6	0.987	
MAT-1037	3	1			
		2	187.6	0.288	
MAT-1038	1	1	15.99		8.000
		2	109.5	0.535	
MAT-1038	2	1	22.98		7.860
		2	119.6	1.08	
MAT-1038	3	1	175.0	7.39	1.560
		2	132.4	2.08	
MAT-1039	1	1	22.77	0.159	8.744
		2	170.7	1.05	
MAT-1039	2	1	21.41	0.294	8.465
		2	164.1	0.452	
MAT-1039	3	1	12.17		8.698
		2	173.9	1.16	
MAT-1039	4	1	43.67	0.102	7.658
		2	162.9	2.50	
MAT-1041	1	1	14.25		8.222
		2	172.6		
MAT-1041	2	1	11.24		8.285
		2	165.3		
MAT-1041	3	1	176.89	4.05	3.508
		2	238.7	0.0692	
MAT-1042	1	1	6.653		7.974
		2	162.4	0.272	
MAT-1042	2	1	54.17	0.0727	2.807
		2	37.67	0.100	
MAT-1043	1	1	116.17	0.513	5.064
		2	185.6	1.10	
MAT-1043	2	1	150.4		3.606
		2	153.9	2.75	
MAT-1043	3	1	45.92	0.0571	7.519
		2	162.8	1.09	

MAT-1044	1	1	9.507		7.857
		2	158.3	0.854	
MAT-1044	2	1	47.07	0.00562	7.078
		2	172.3	0.618	
MAT-1044	3	1	52.67	0.0985	6.957
		2	156.5	1.00	

Table II on the prior pages, much like Table I, provides the sample name, melt cycle, and delay time between recalescence events for the $Co_{60}Si_{40}$ alloy. It also displays the calculated undercooling and solidification velocities for each respective recalescence event. Blank cells indicate a lack of data or an omission of bad data and red velocity values indicate nucleation on the back surface.

4.2 Undercooling and delay time analysis techniques

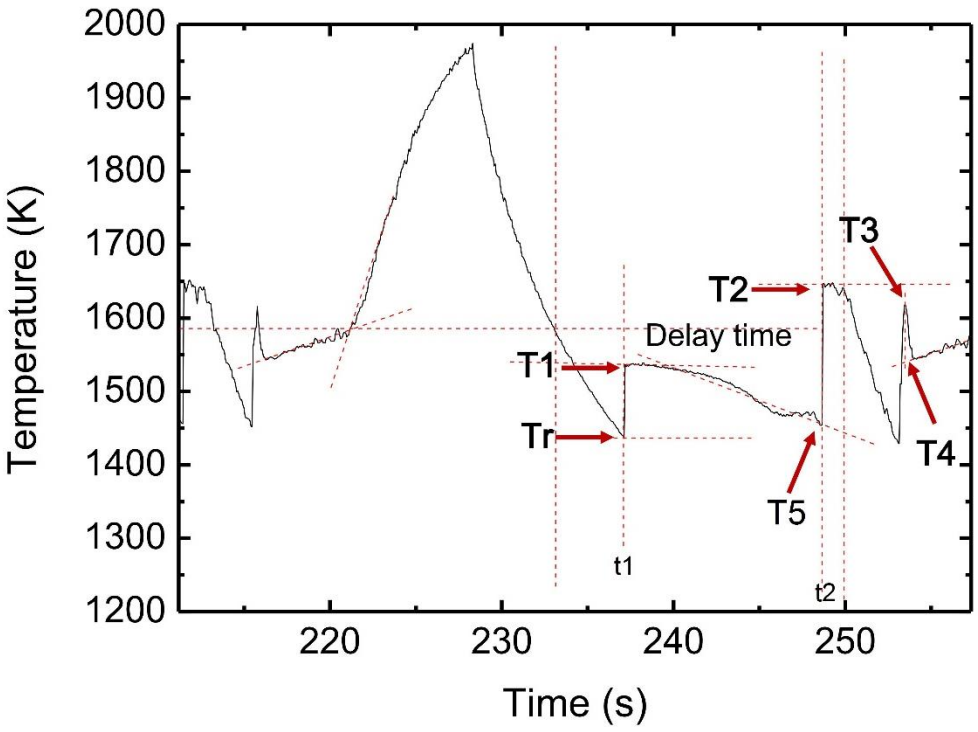

Figure 5: Time-temperature graph for a $Co_{60}Si_{40}$ melt cycle

The delay times and undercoolings for each melt cycle were found by plotting their respective time-temperature graphs. An example of one for a $Co_{60}Si_{40}$ sample is shown above in Figure 5. Between 216 and 227 seconds into the test, the sample is heated with a laser as described in section 3.2. The first slope shows the heating of the sample while in the solidus phase. The change in slope signifies that the sample has completely liquefied, and the intersection of the two slopes represents the liquidus temperature. Temperature graphs were calibrated using a pyrometer correction equation to a known value of T_{liq} = 1585 K for $Co_{38.5}Si_{61.5}$ [8] and T_{liq} = 1578 K for $Co_{60}Si_{40}$ [7] from this point:

$$\frac{1}{T} = \left(\frac{1}{T_P}\right) + \left(\frac{1}{T_L} - \frac{1}{T_{LP}}\right) \quad (1)$$

T_P is the uncorrected pyrometer temperature, T_{LP} is the observed pyrometer reference liquidus, or the value of the temperature at the intersection of the slopes, T_L is the known liquidus temperature, and T is the true temperature [21].

Using the labels from Figure 5, the first recalescence undercooling was calculated by subtracting T_r from T_1. The emissivity of the pyrometer was set to a constant 0.25 during experimentation. However, during the second recalescence event, the true emissivity of the sample sometimes changed due to a difference in surface roughness or new phase formation, resulting in falsely high temperature readings for the second recalescence undercooling. These were accounted for by subtracting the spike in the graph after the second recalescence ($T_3 – T_4$), which was understood to be the reverse of the prior emissivity shift as the sample remelted, from the initial undercooling measurement ($T_2 – T_5$). The delay time between recalescence events was found by subtracting t_1 from t_2.

4.3 Velocity analysis techniques

The solidification velocity was measured using a MATLAB GUI developed by Justin Rodriguez. The software allows the user to step through a recalescence event frame by frame.

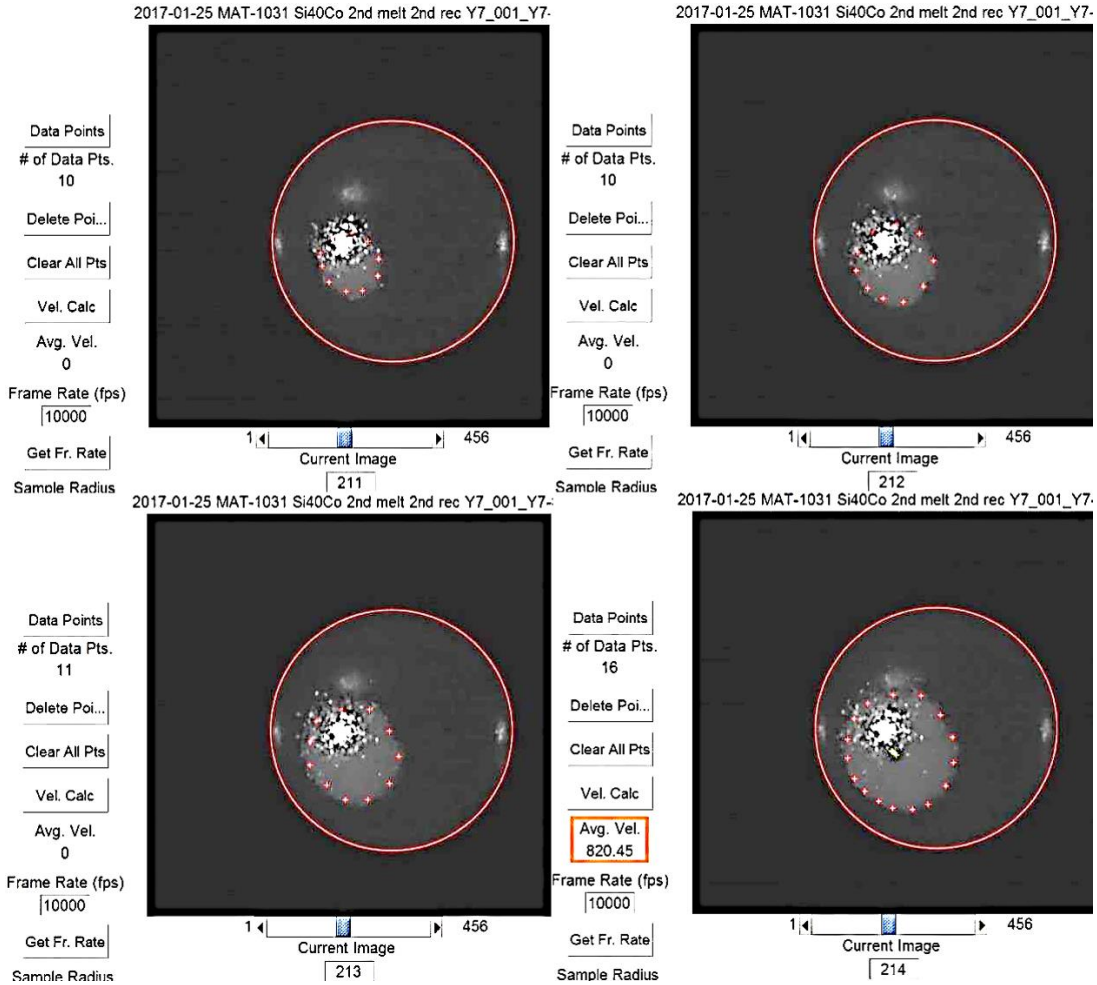

Figure 6: Solidification velocity analysis

Figure 6 above illustrates the process of retrieving velocity data. In this example, the second recalescence nucleates on the front surface. The velocity is tracked by selecting points on the edge of the growing phase in successive frames. As the framerate, radius of the sample in pixels, and radius of a calibration sphere in pixels and meters are known, the growth velocity can be calculated. The orange-boxed value in the lower

right quadrant is the calculated velocity in radii/s, which is converted to m/s by multiplying by the radius in units of meters. The yellow points shown in the bottom-right image are the extrapolated nucleation sites for each set of points within a frame – a precise grouping implies accuracy of the calculation, as a constant nucleation site is assumed during calculations.

Nucleations occurring on the front surface provided the best results. Due to the fractal nature of dendrite formation, apparent solidification velocity can change based on the branching of the dendrites. The most accurate solidification velocity is thus determined immediately after nucleation. For this reason, nucleation events on the back surface of the sample were ignored, as not only were they harder to analyze, but also too much time had passed before the phase appeared on the front surface for any results gathered to be considered accurate.

5 Discussion

5.1 $Co_{38.5}Si_{61.5}$ solidification pathways

The results of this experiment provide evidence for multiple temperature-dependent solidification paths in both CoSi systems studied. With regards to $Co_{38.5}Si_{61.5}$, prior studies by Yao [5], Zhang [3], and Li [8] suggested CoSi was the primary phase to form. A critical undercooling temperature ΔT_c of 88 K [3] and 75 K [8] was found, below which CoSi formed first and above which $CoSi_2$ formed first. This study averaged the ΔT_c value to 81.5 K. Several relationships were evaluated in order to provide supporting or contrasting evidence for prior conclusions. In the following graphs, vertical lines at ΔT_c = 81.5 K along the first recalescence undercooling axis represent the critical undercooling of the alloy. A horizontal line at T_{liq} = 1585 K indicates the liquidus temperature of the alloy.

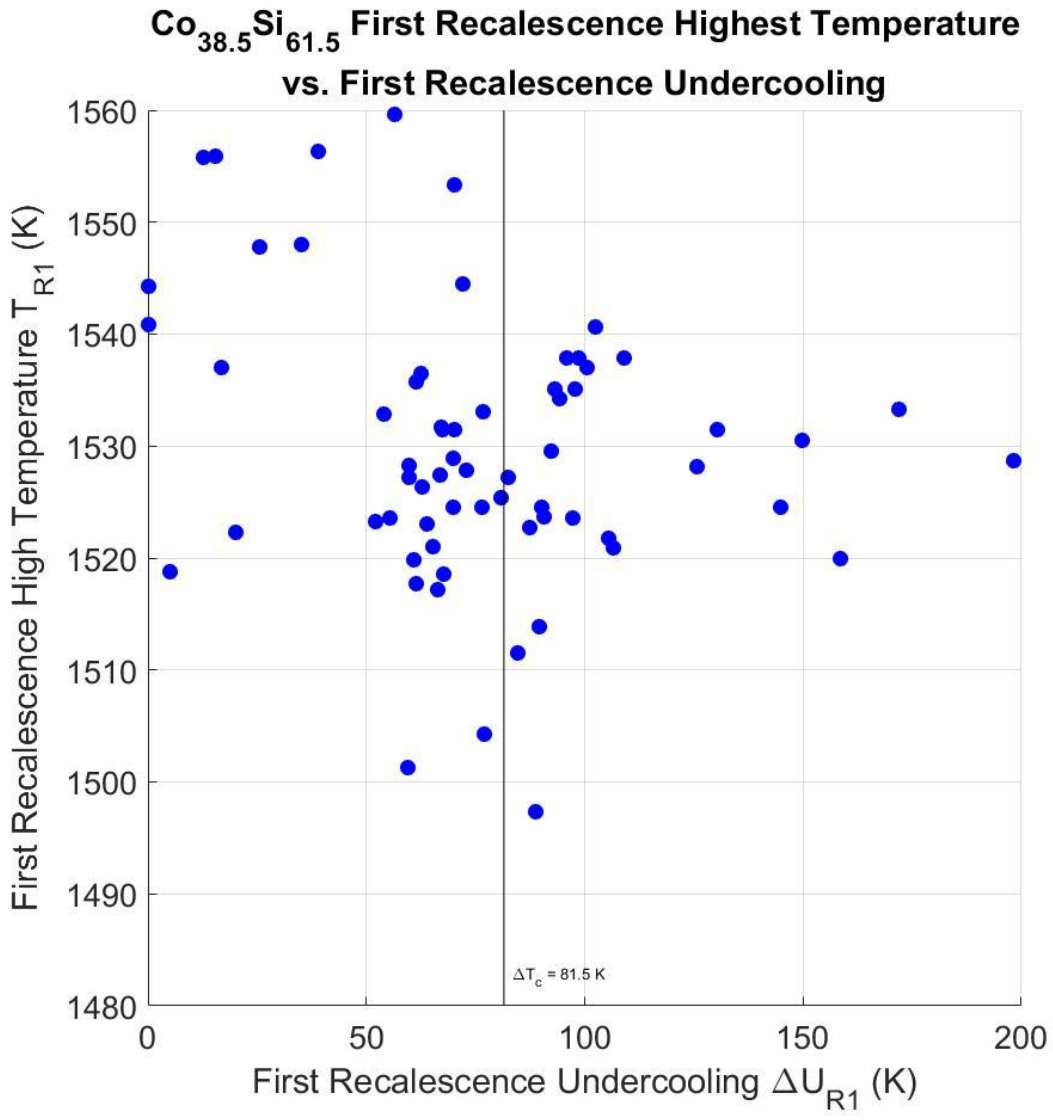

Figure 7: Highest temperature reached during the first recalescence event vs. the first recalescence undercooling for the $Co_{38.5}Si_{61.5}$ system

Figure 7 above indicates no relationship between the highest temperature observed during the first recalescence event (T_{R1}) and the first recalescence undercooling (ΔU_{R1}) for the $Co_{38.5}Si_{61.5}$ alloy. No first recalescence brought the temperature of the sample back to T_{liq} (1585 K).

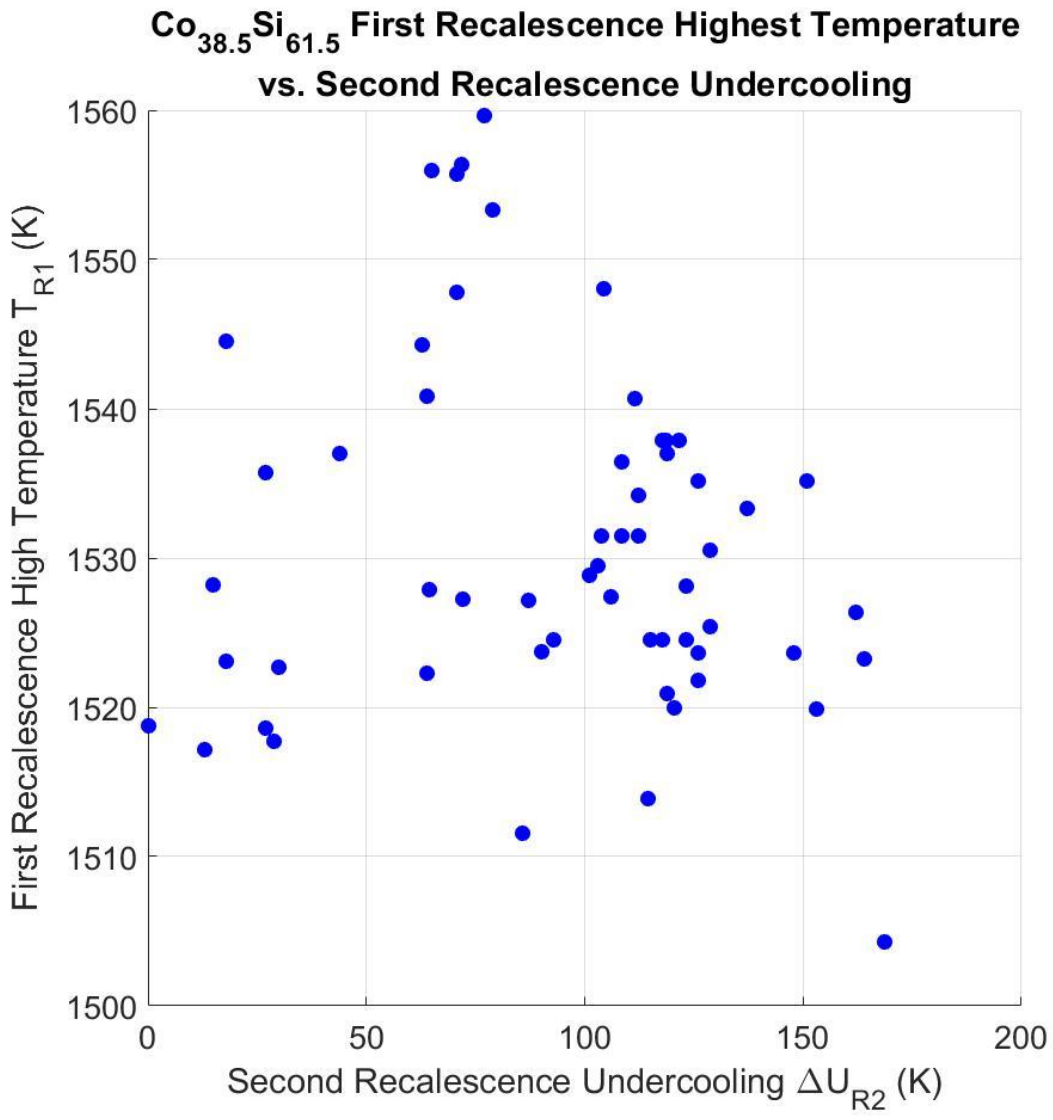

Figure 8: Highest temperature reached during the first recalescence event vs. the second recalescence undercooling for the $Co_{38.5}Si_{61.5}$ system

There was also no clear relationship between T_{R1} and the second recalescence undercooling (ΔU_{R2}). However, high T_{R1} values were only attained at lower ΔU_{R2} values. This is probably because higher T_{R1} values bring the temperature of the sample closer to T_{liq}, the expected temperature after second recalescence. When the sample undergoes a second recalescence, it has less of a temperature difference to compensate for than a sample with a low T_{R1} would have.

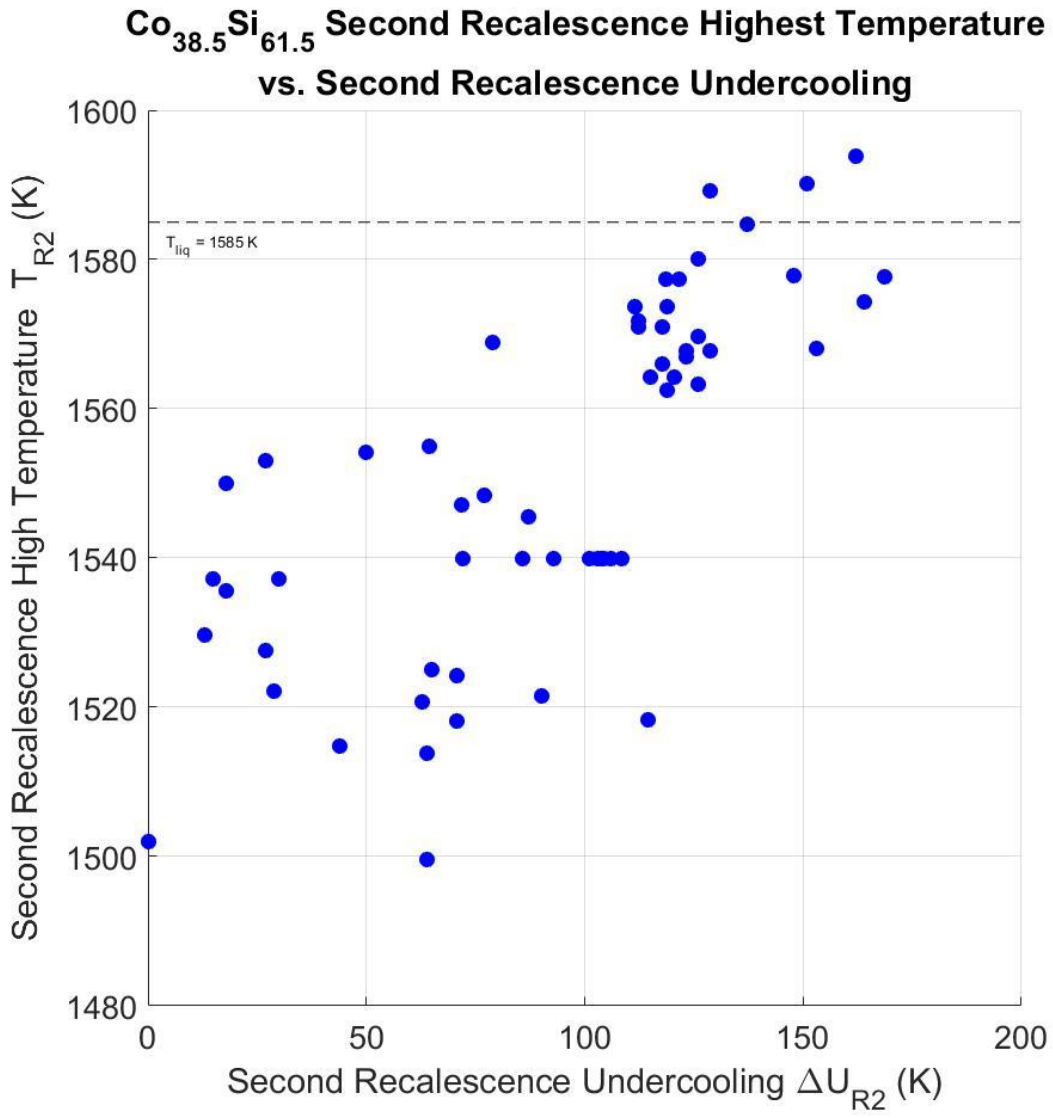

Figure 9: Highest temperature reached during the second recalescence event vs. the second recalescence undercooling for the $Co_{38.5}Si_{61.5}$ system

Figure 9 above shows a general increasing trend between the highest temperature observed in the second recalescence event (T_{R2}) and ΔU_{R2} in the $Co_{38.5}Si_{61.5}$ system.

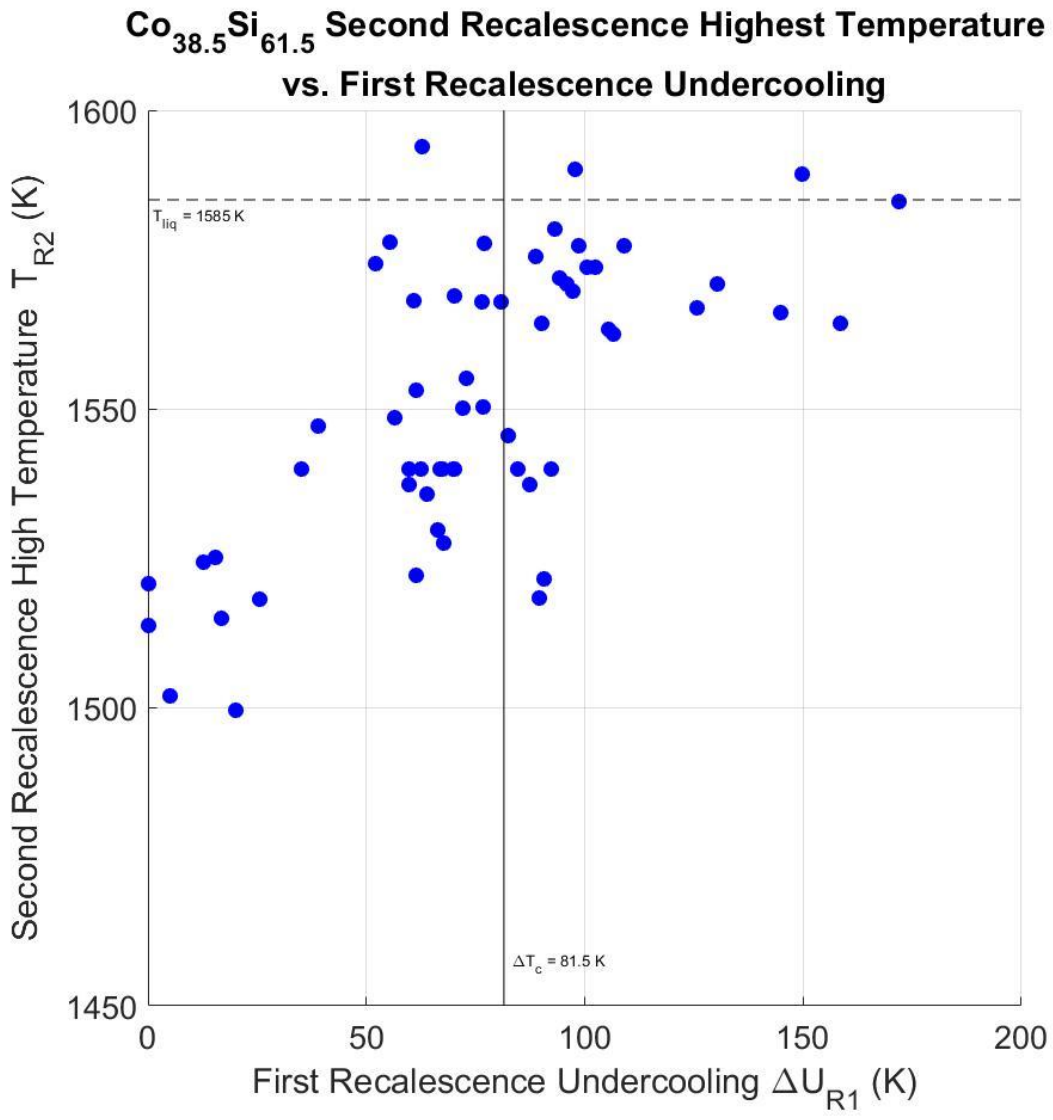

Figure 10: Highest temperature reached during the second recalescence event vs. the first recalescence undercooling for the $Co_{38.5}Si_{61.5}$ system

Figure 10 also shows an increasing trend between T_{R2} and $\Delta U_{R1.}$ The splitting that ΔT_c creates suggests that the primary CoSi phase pathway does not recalesce to as high a temperature during secondary phase formation as does the primary $CoSi_2$ phase.

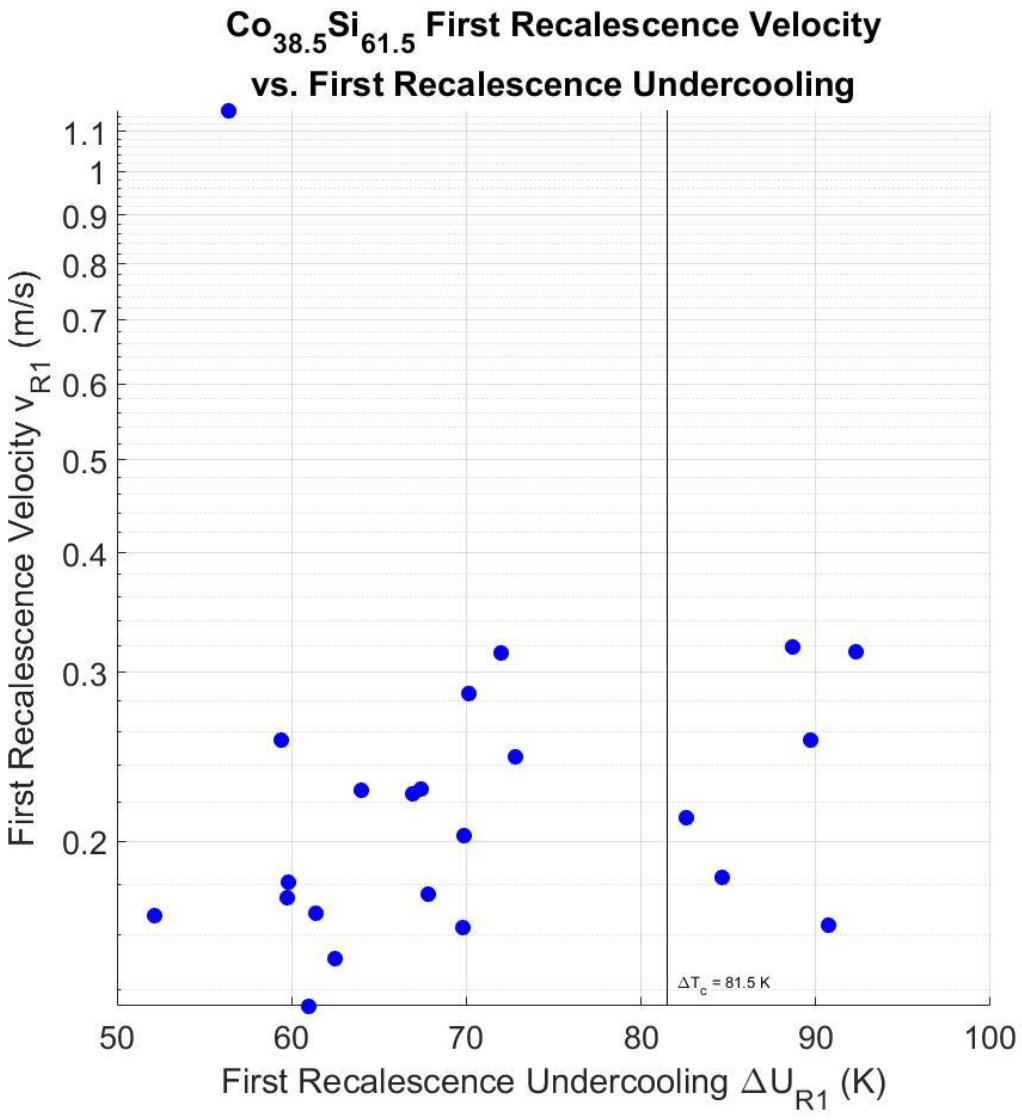

Figure 11: First recalescence solidification velocity vs. the first recalescence undercooling for the $Co_{38.5}Si_{61.5}$ system

Figure 11 above shows two distinct regions when first recalescence solidification velocity (v_{R1}) is plotted against ΔU_{R1}. Below ΔT_c, CoSi forms the primary phase. Above ΔT_c, $CoSi_2$ forms the primary phase. CoSi generally solidifies faster than $CoSi_2$ [3], but its respective grouping does not show a larger velocity than that of the $CoSi_2$ in this study.

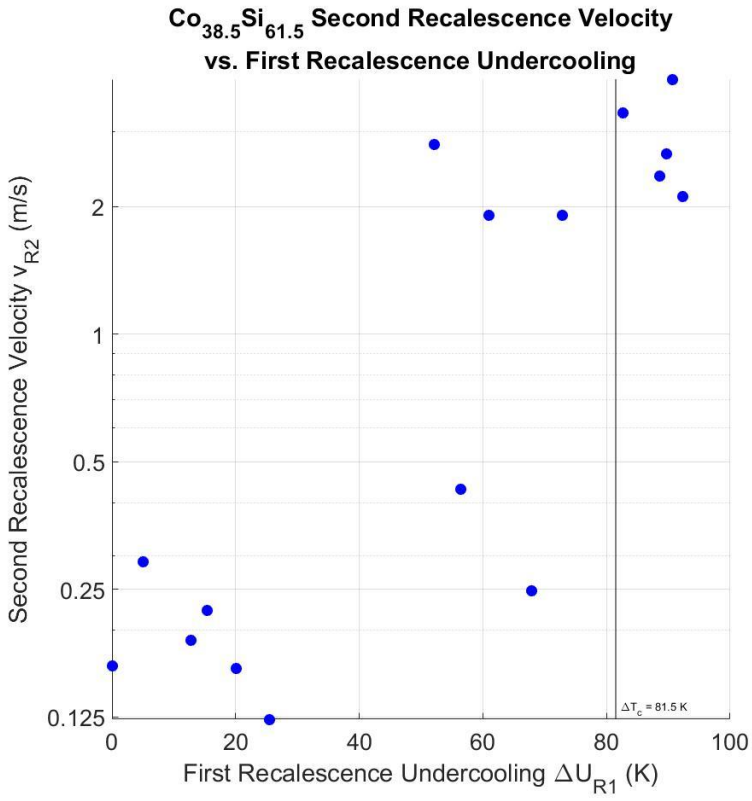

Figure 12: Second recalescence solidification velocity vs. the first recalescence undercooling for the $Co_{38.5}Si_{61.2}$ system

Plotting second recalescence solidification velocity (v_{R2}) against ΔU_{R1} again shows two distinct groups. Li et. Al. [8] proposed that at high undercoolings, the $CoSi_2$ phase is followed by the CoSi phase during the second recalescence. At low undercoolings where the $CoSi_2$ nucleation is largely subdued, eutectic grains and $CoSi_2$ halos form [8] [3]. It would be expected, then, that the formation of CoSi would occur at a faster rate than those of the formation of eutectic grains and $CoSi_2$. Figure 12 then supports the theory that CoSi forms below ΔT_c with remelting upon second recalescence forming eutectic grains and $CoSi_2$ halos and that $CoSi_2$ forms above ΔT_c, followed by CoSi during the second recalescence. The points in the lower left correspond to a CoSi primary phase, and those in the upper right correspond to a $CoSi_2$ primary phase. The value of ΔT_c, however, does appear to be a few degrees too high.

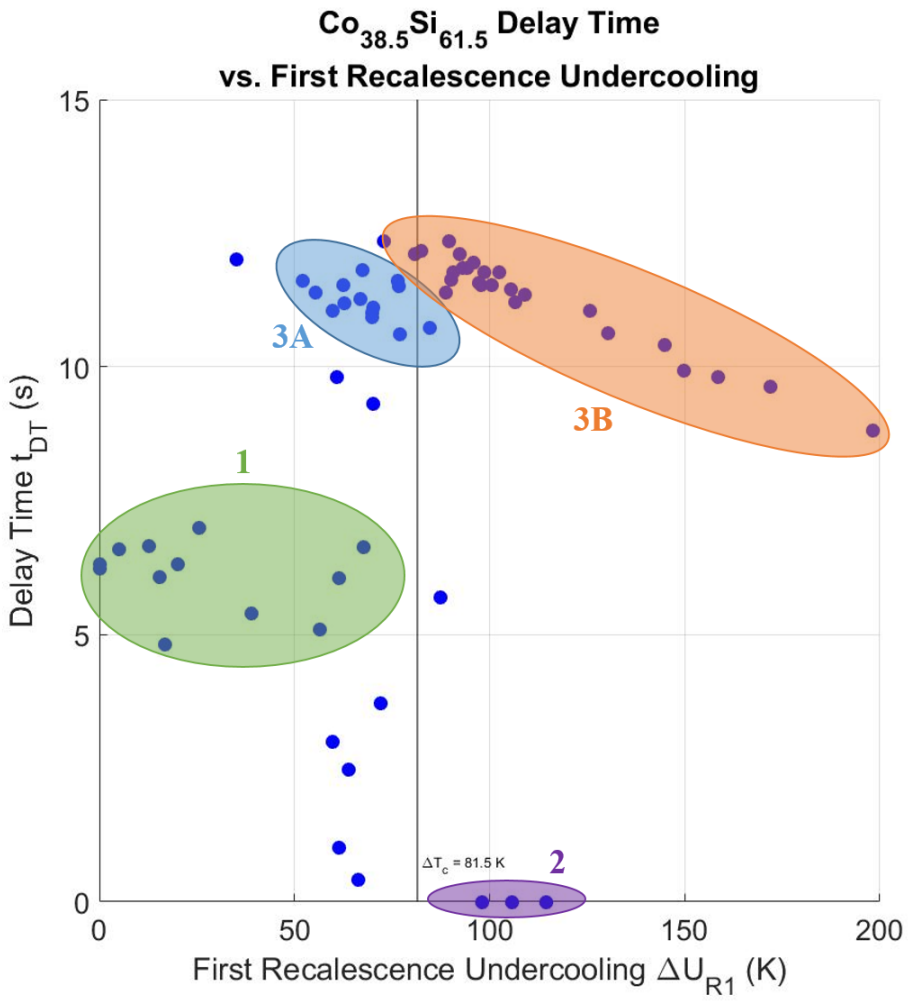

Figure 13: Delay time between recalescence events vs. the first recalescence undercooling for the $Co_{38.5}Si_{61.5}$ system

Figure 13 displays the delay time between recalescence events (t_{DT}) as a function of ΔU_{R1}. Again, two groups can easily be distinguished with ΔT_c providing a general separator. The delay time seen where $CoSi_2$ solidifies primarily indicates that CoSi has difficulty nucleating out of the $CoSi_2$ phase. This long delay time could also promote growth of a metastable phase as suggested by the Li manuscript [8]. A metastable phase was found to grow during long delay times in the $Co_{60}Si_{40}$ alloy [7]. Upon closer inspection, however, four groups have been identified. Region 1 in green identifies the points where the CoSi phase has been suggested to nucleate primarily.

Region 2 in purple identifies the undercooling range of samples that recalesced only once, meaning there was no delay time. Regions 3A in blue and 3B in orange separate the grouping where $CoSi_2$ solidifies primarily into two groups with similar but shifted t_{DT} vs. ΔU_{R1} relationships. Samples from each of these regions were identified and subject to metallographic analysis.

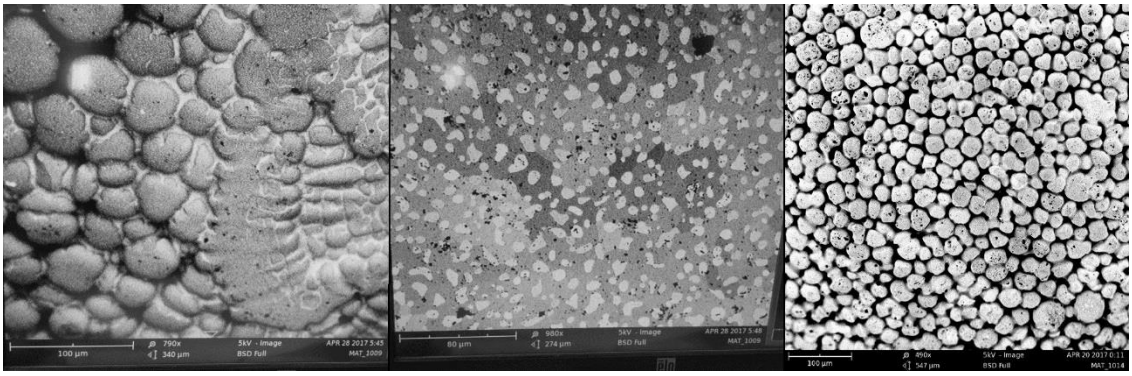

Figure 14: Metallography of $Co_{38.5}Si_{61.5}$ regions 1 (L), 2 (M), and 3A and 3B (R) [22]

Figure 14 displays surface images of samples belonging to regions 1, 2, and 3A and 3B of Figure 13. The leftmost figure shows a coarse dendritic structure, corresponding to region 1. The middle figure shows an anomalous eutectic structure, corresponding to region 2. Regions 3A and 3B show a fine dendritic structure coarsened to appear cellular. These images show that the delay shift observed in Figure 13 relates to a morphology change. These results appear consistent with CoSi and $CoSi_2$ growth as discussed by Zhang [3] and Li [8] and synchrotron data found by Shuleshova [20], but elemental analysis is required for confirmation within this study.

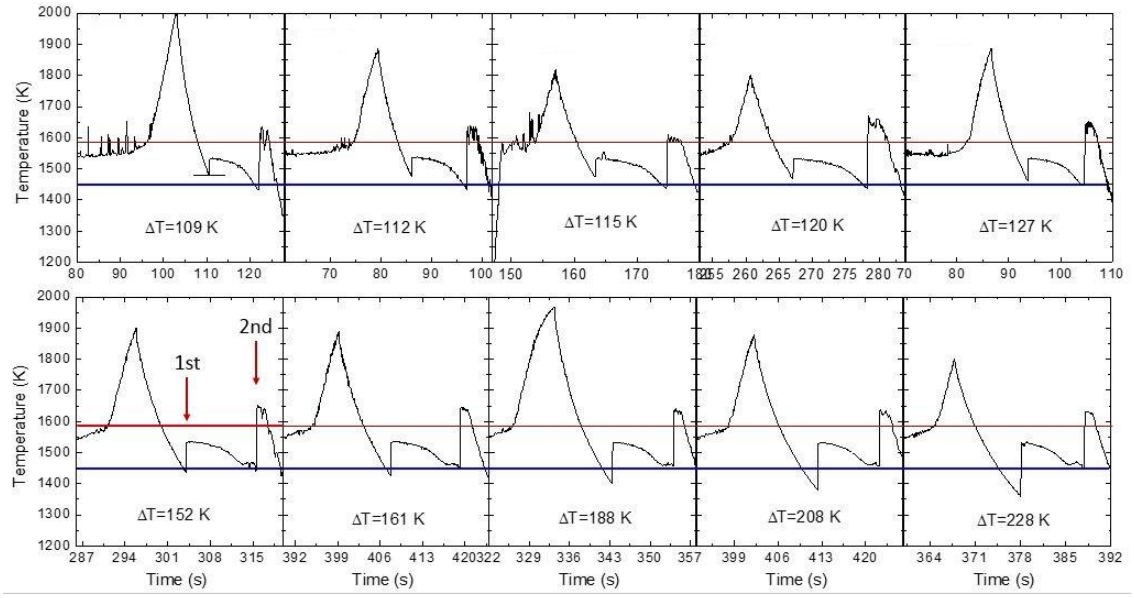

Figure 15: Difference in temperature profile of $Co_{38.5}Si_{61.5}$ regions 3A (T) and 3B (B) [22]

Compared to the first recalescence undercoolings of region 3B, those of region 3A are small. There is also no small plateau, or "hump," just before the second recalescence. The first recalescence undercoolings of region 3B are large, falling below a critical undercooling temperature of 1450 K marked by the horizontal blue lines. The hump before second recalescence prevents deeper undercoolings, resulting in hotter temperatures at second recalescence than in region 3A. The slope of the delay time versus first recalescence undercooling as seen in Figure 13 is consistent in regions 3A and 3B, and the shift between them is related to the association between hotter temperatures and longer delay times.

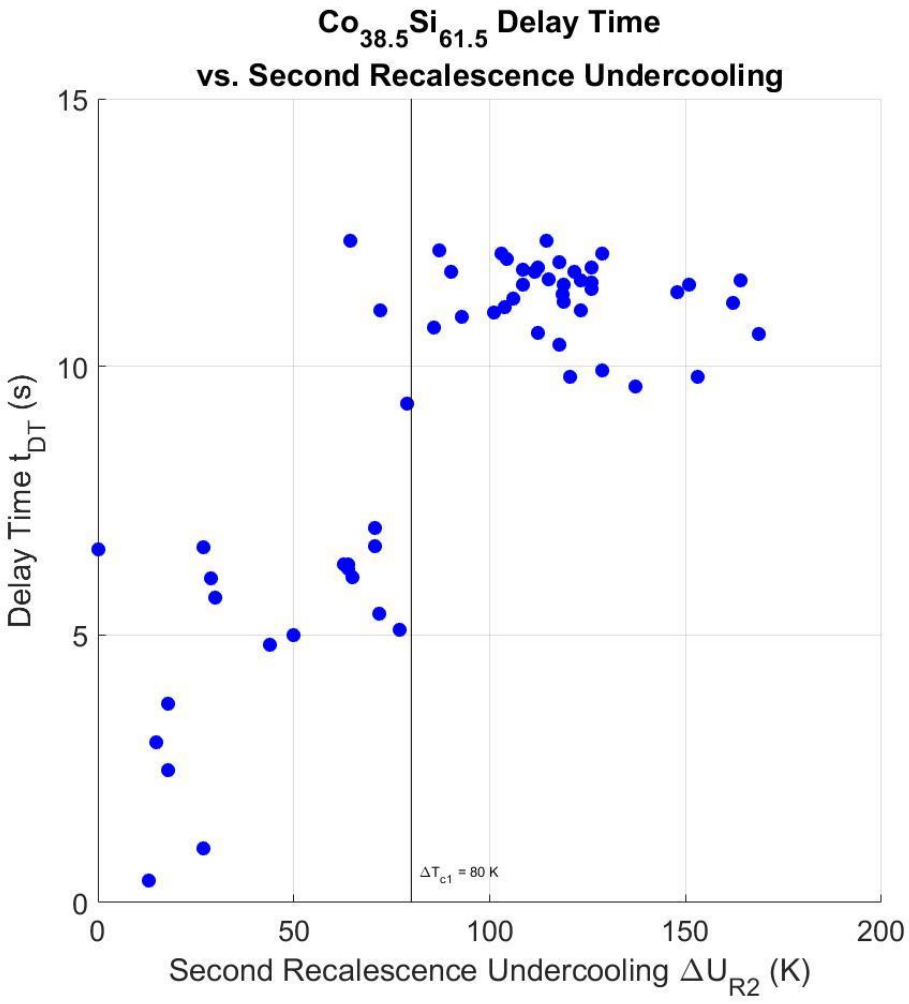

Figure 16: Delay time between recalescence events vs. the second recalescence undercooling for the $Co_{38.5}Si_{61.5}$ system

Similar groupings to those in Figure 13 are seen above in Figure 16, where t_{DT} is plotted against ΔU_{R2}. Longer delay times grant more time for the sample to cool, so it is expected that they correspond to deeper undercoolings. However, the secondary CoSi phase following the primary $CoSi_2$ does not appear to form until a ΔU_{R2} of roughly 80 K is reached. It could be that only at this undercooling is the energy barrier for nucleation reduced enough for CoSi to crystallize. The labeled ΔT_c in Figures 16 above and 17 below can then be understood to be the critical undercooling necessary for the second phase to form from a primary $CoSi_2$ solid.

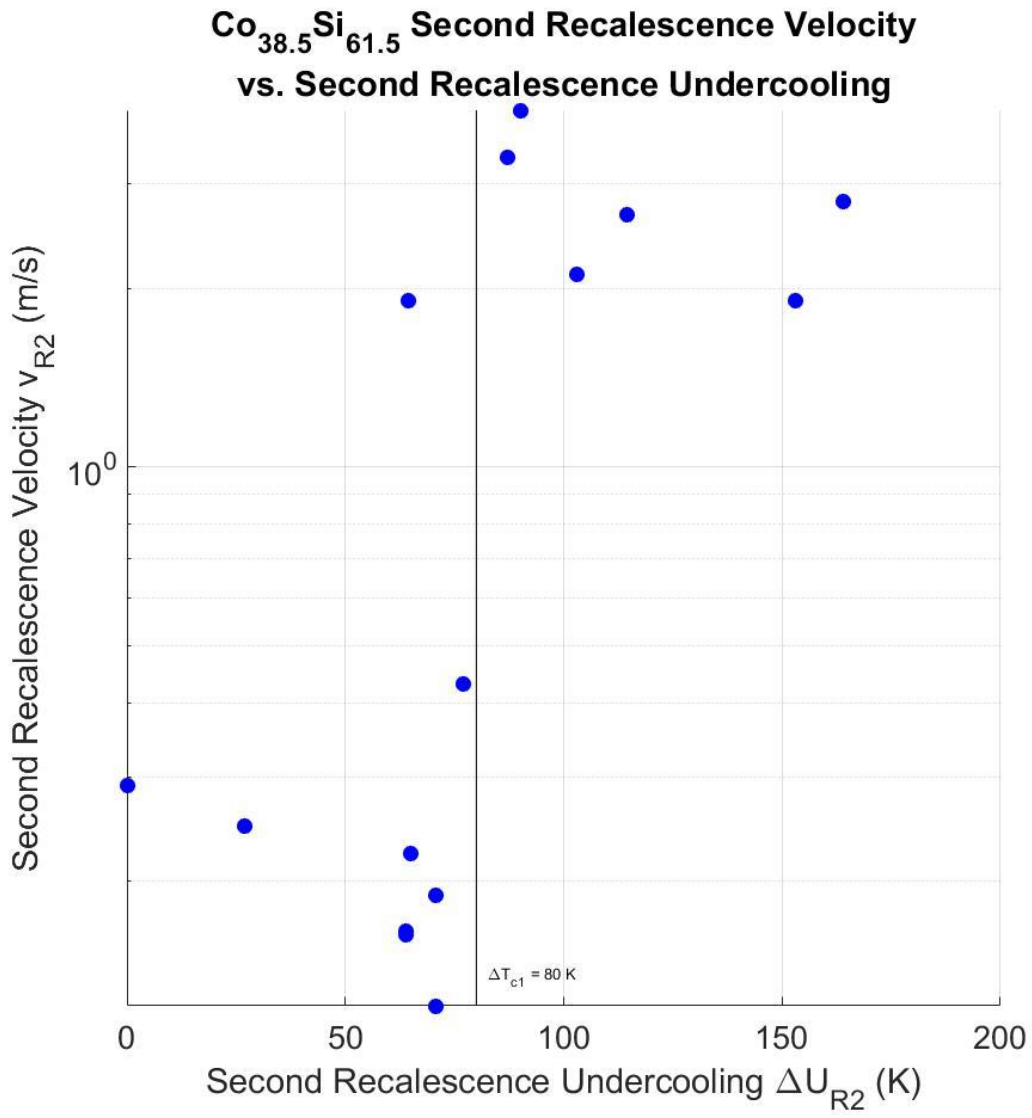

Figure 17: Second recalescence solidification velocity vs. the second recalescence undercooling for the $Co_{38.5}Si_{61.5}$ system

Figure 12 showed that the points with high v_{R2} values correspond to a primary $CoSi_2$/secondary CoSi pathway. Plotting v_{R2} against ΔU_{R2} in Figure 17 then indicates a CoSi secondary phase does not nucleate until a critical undercooling temperature of $\Delta T_c = 80$ K is reached, as the secondary CoSi phase is grouped in the upper right.

5.2 Co60Si40 solidification pathways

Data from Wang et. al. [7] is superimposed over that gathered during this experiment in several of the following plots. That paper, as well as one published by Yao et. al. [5] suggest that CoSi forms the primary solid during first recalescence. Wang et. al. found two critical undercoolings of ΔT_{c1} = 50 K and ΔT_{c2} = 90 K. Between the two, the stable β-Co_2Si/CoSi eutectic was found to crystallize first, and above ΔT_{c2} the metastable α-Co_2Si/CoSi became the primary solid. As in section 5.1, several relationships were evaluated in order to provide supporting or contrasting evidence for the prior conclusions. The critical undercoolings are again represented by vertical lines on the first recalescence undercooling axes in the following figures. Horizontal lines on temperature axes at 1578 K, 1559 K, and 1511 K locate the liquidus temperature (T_{liq}), the eutectic temperature (T_E), and the eutectoid temperature (T_{Ed}) respectively.

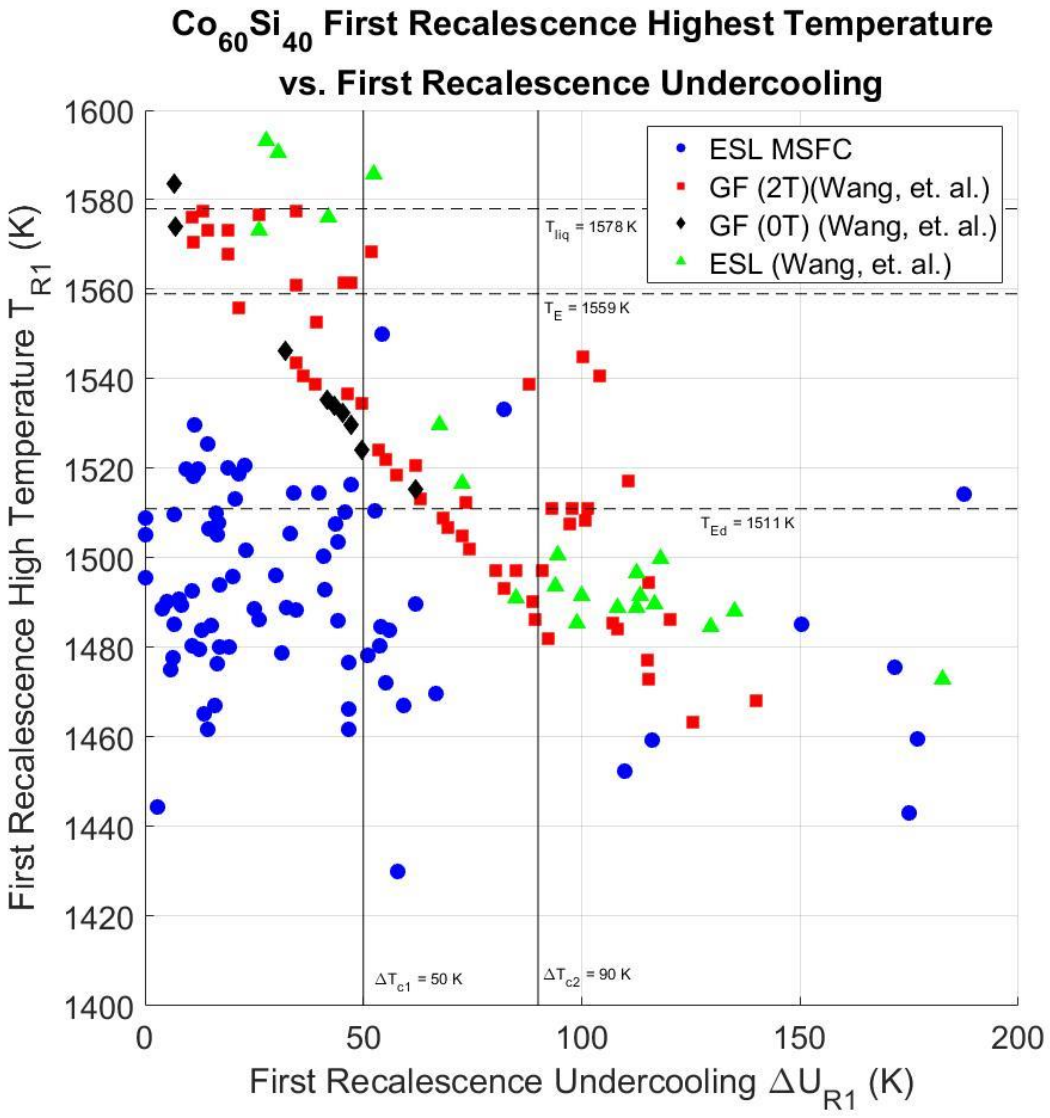

Figure 18: Highest temperature reached during the first recalescence event vs. the first recalescence undercooling for the $Co_{60}Si_{40}$ system

Figure 18 above indicates no relationship between T_{R1} and ΔU_{R1} for the $Co_{60}Si_{40}$ alloy. These findings contradict those of Wang, et. al, who show that undercoolings inversely relate to high temperatures observed.

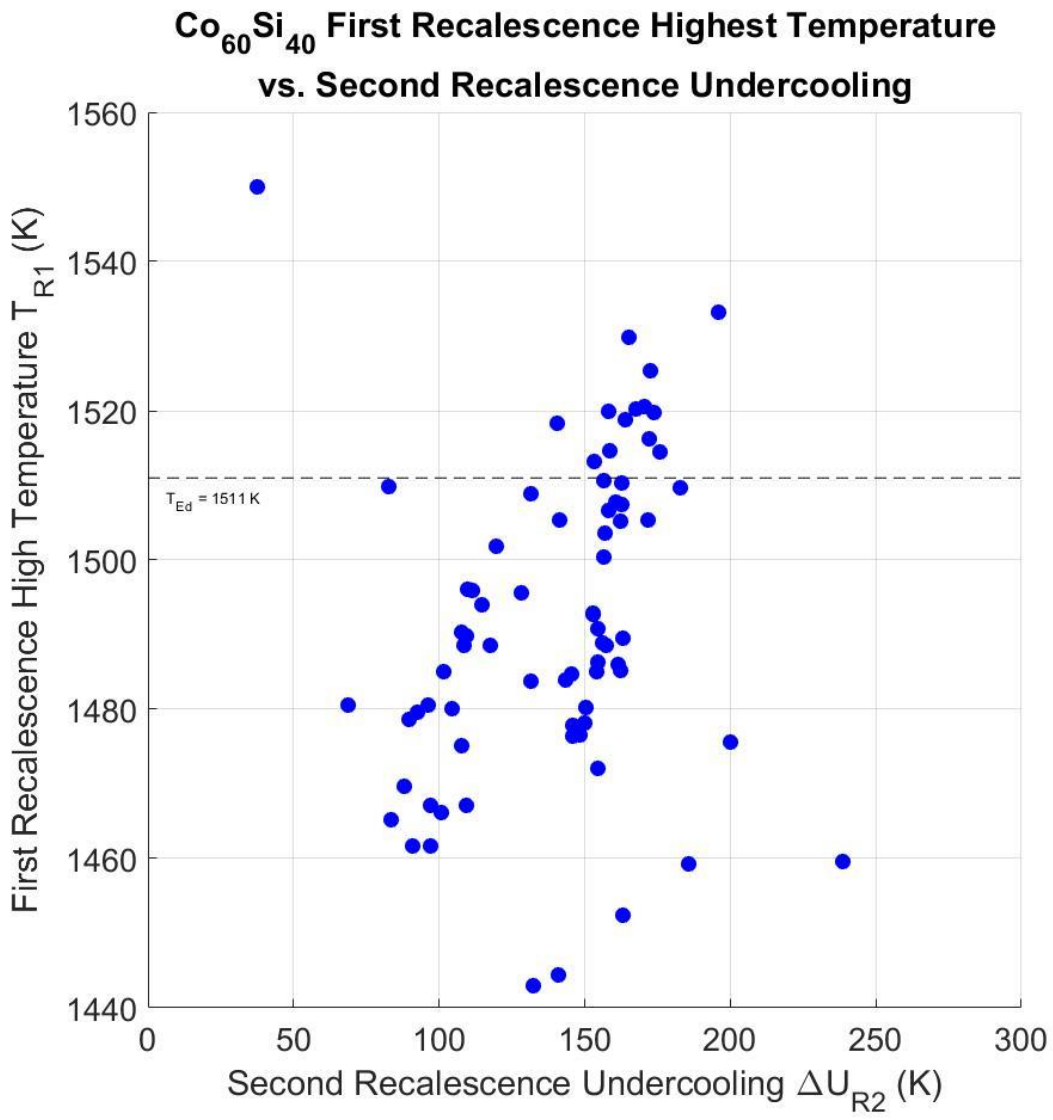

Figure 19: Highest temperature reached during the first recalescence event vs. the second recalescence undercooling for the $Co_{60}Si_{40}$ system

Figure 19 shows an increasing trend between T_{R1} and ΔU_{R2}. No such trend was observed in Figure 8, which shows the same relationship for the $Co_{38.5}Si_{61.5}$ alloy.

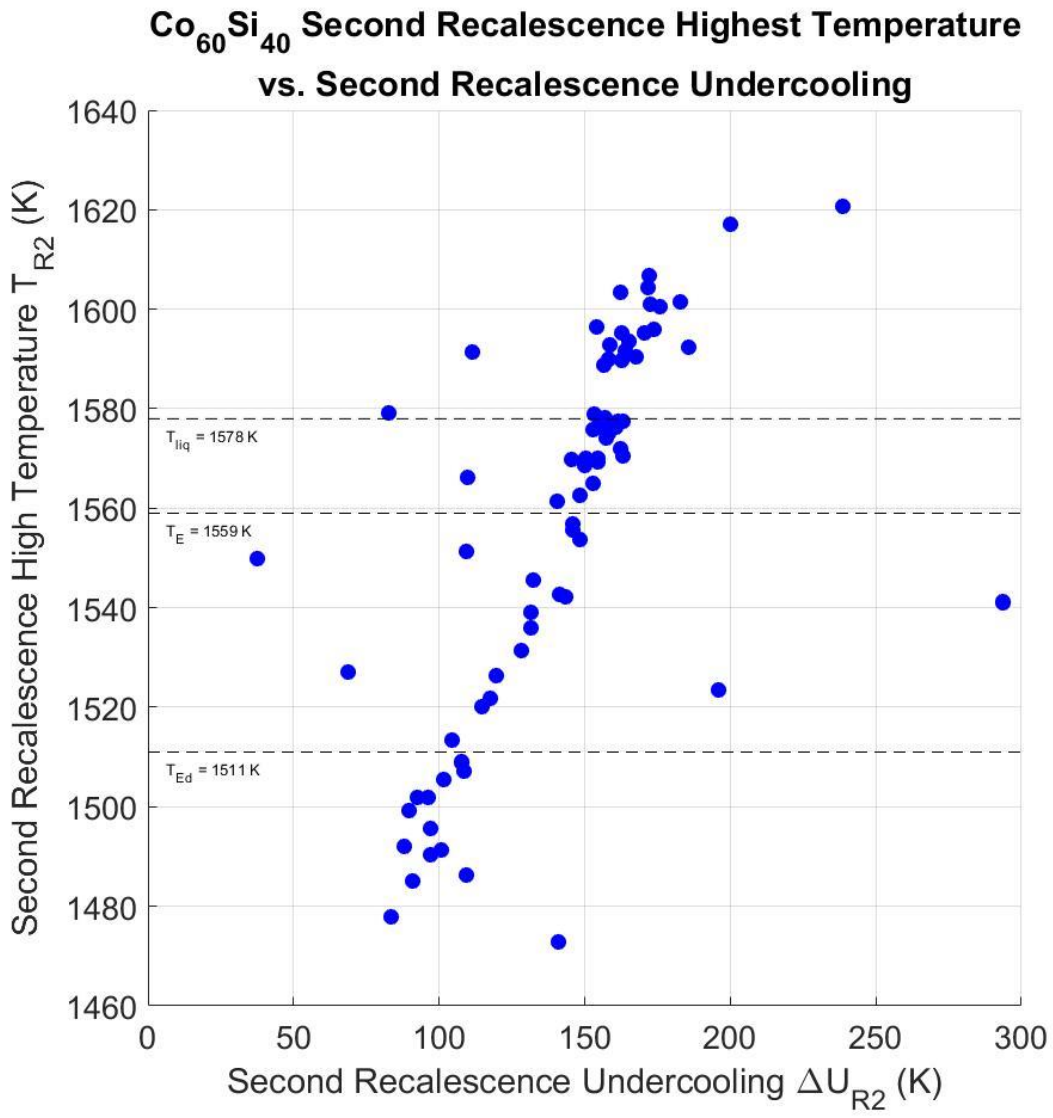

Figure 20: Highest temperature reached during the second recalescence event vs. the second recalescence undercooling for the $Co_{60}Si_{40}$ system

Figure 20 above shows a linearly increasing relationship between T_{R2} and ΔU_{R2}. Again, a similar relationship was found for the $Co_{38.5}Si_{61.5}$ alloy (Figure 9). This extremely strong correlation indicates the limits of the metastable extension into the equilibrium phase diagram.

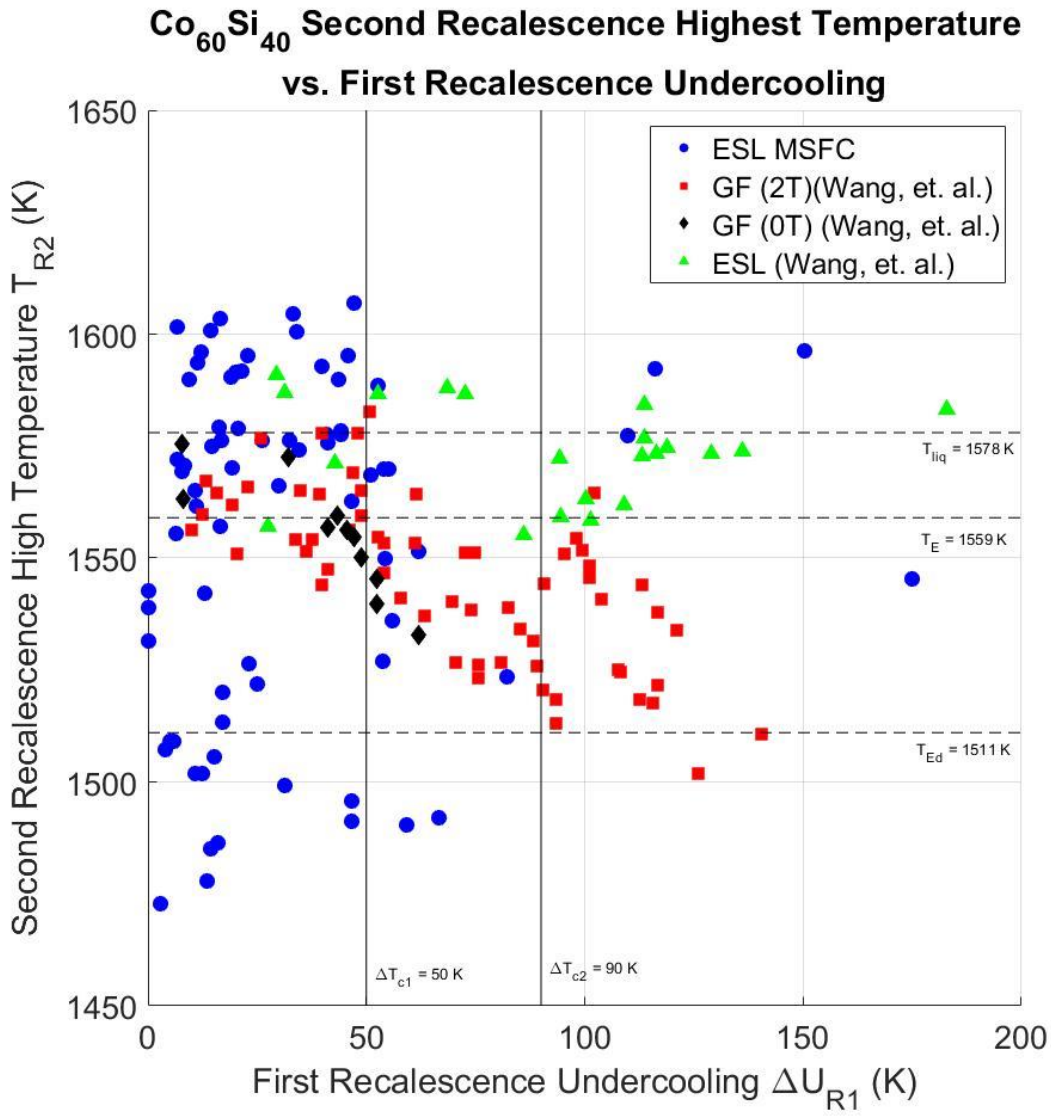

Figure 21: Highest temperature reached during the second recalescence event vs. the first recalescence undercooling for the $Co_{60}Si_{40}$ system

Data gathered during this experiment seems to show no relationship between T_{R2} and ΔU_{R1}, despite the downward trend observed by Wang et. al.

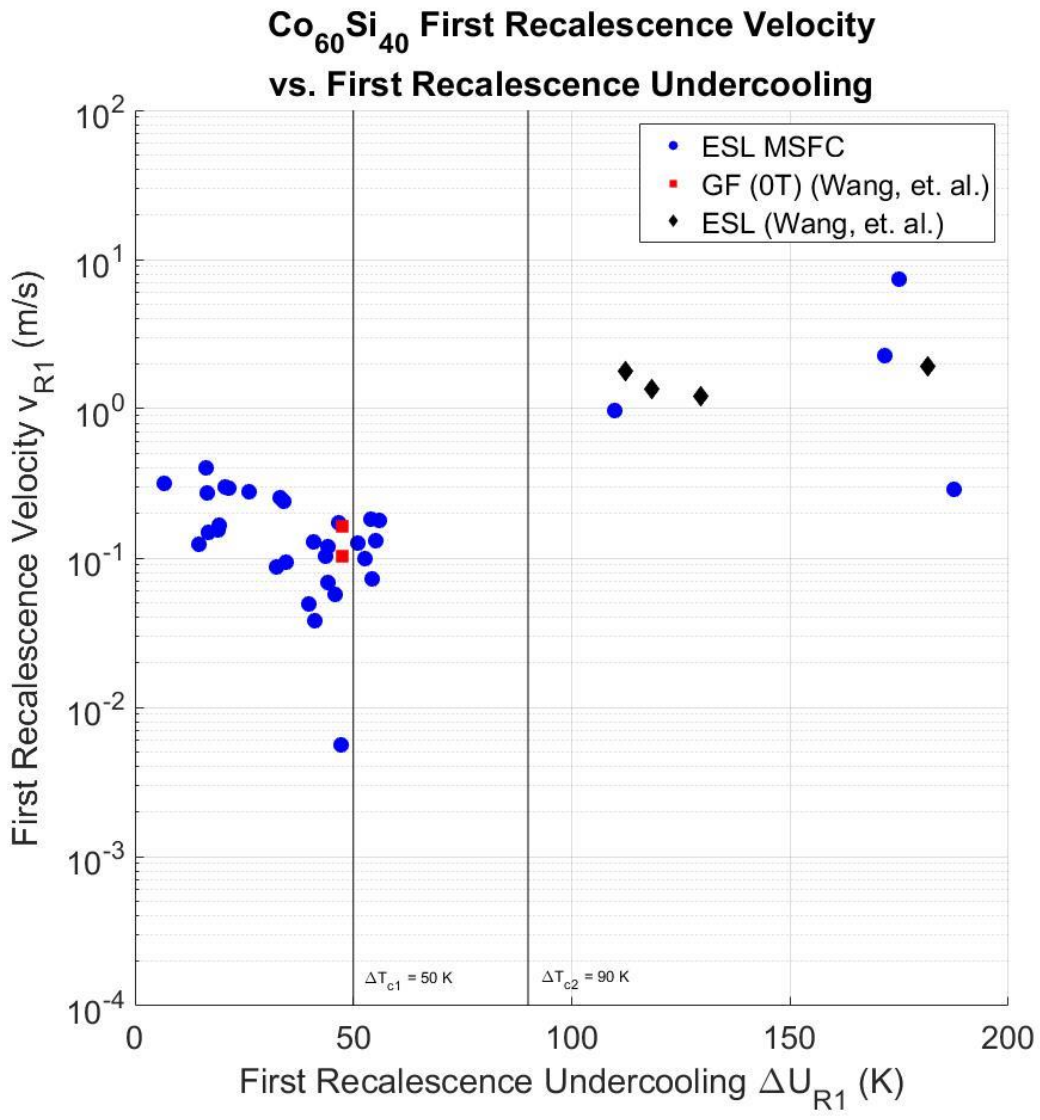

Figure 22: First recalescence solidification velocity vs. the first recalescence undercooling for the $Co_{60}Si_{40}$ system

Plotting v_{R1} against ΔU_{R1} attempted to show distinct groupings within each section split by the critical undercoolings. However, only the primary CoSi phase appears due to a lack of data – the $Co_{60}Si_{40}$ samples were difficult to undercool to low temperatures. As Wang proposed a slower growth of the β-Co_2Si/CoSi phase than the CoSi phase, a grouping between ΔT_{R1} and ΔT_{R2} with generally lower velocities than those of the grouping left of ΔT_{R1} would have provided supporting evidence. The sole

point just left of ΔT_{R1} with an observed v_{R1} of 0.00562 m/s (MAT-1044 melt 2) could have crystallized into the β-Co_2Si/CoSi eutectic, but one data point is nothing to draw conclusions from.

Despite a small grouping in this region, the α-Co_2Si/CoSi phase growth velocity appears to be generally be faster than that of the absent growth velocities of the β-Co_2Si/CoSi phase because the velocities of the former appear to be faster than those of the CoSi phase. As previously discussed, these were expected to in turn be faster than those of the β-Co_2Si/CoSi phase. The deeper undercoolings observed may also indicate a larger driving force behind the formation of the α-Co_2Si/CoSi phase, causing it to grow faster [7]. A prior study by Yasuda et. al. [23] observed the formation of a metastable phase over a stable one at high undercoolings and concluded that there was a difficulty for the stable phase to nucleate. A similar relationship likely occurs with the metastable and stable phases of Co_2Si.

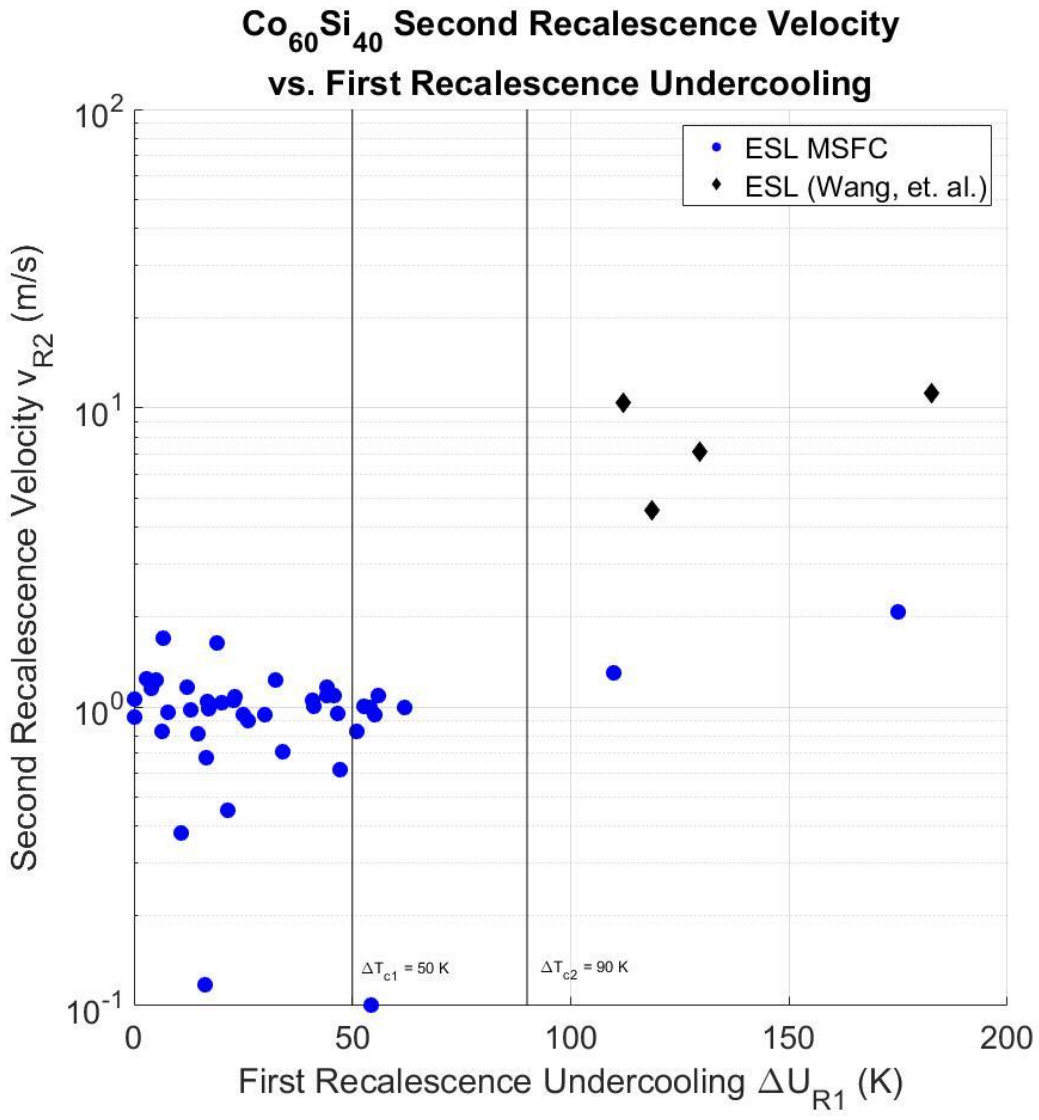

Figure 23: Second recalescence solidification velocity vs. the first recalescence undercooling for the $Co_{60}Si_{40}$ system

A lack of distinct groupings within the primary β-Co_2Si/CoSi phase split and the primary α-Co_2Si/CoSi phase split make it impossible to draw conclusions from Figure 23, which shows v_{R2} as a function of ΔU_{R1}.

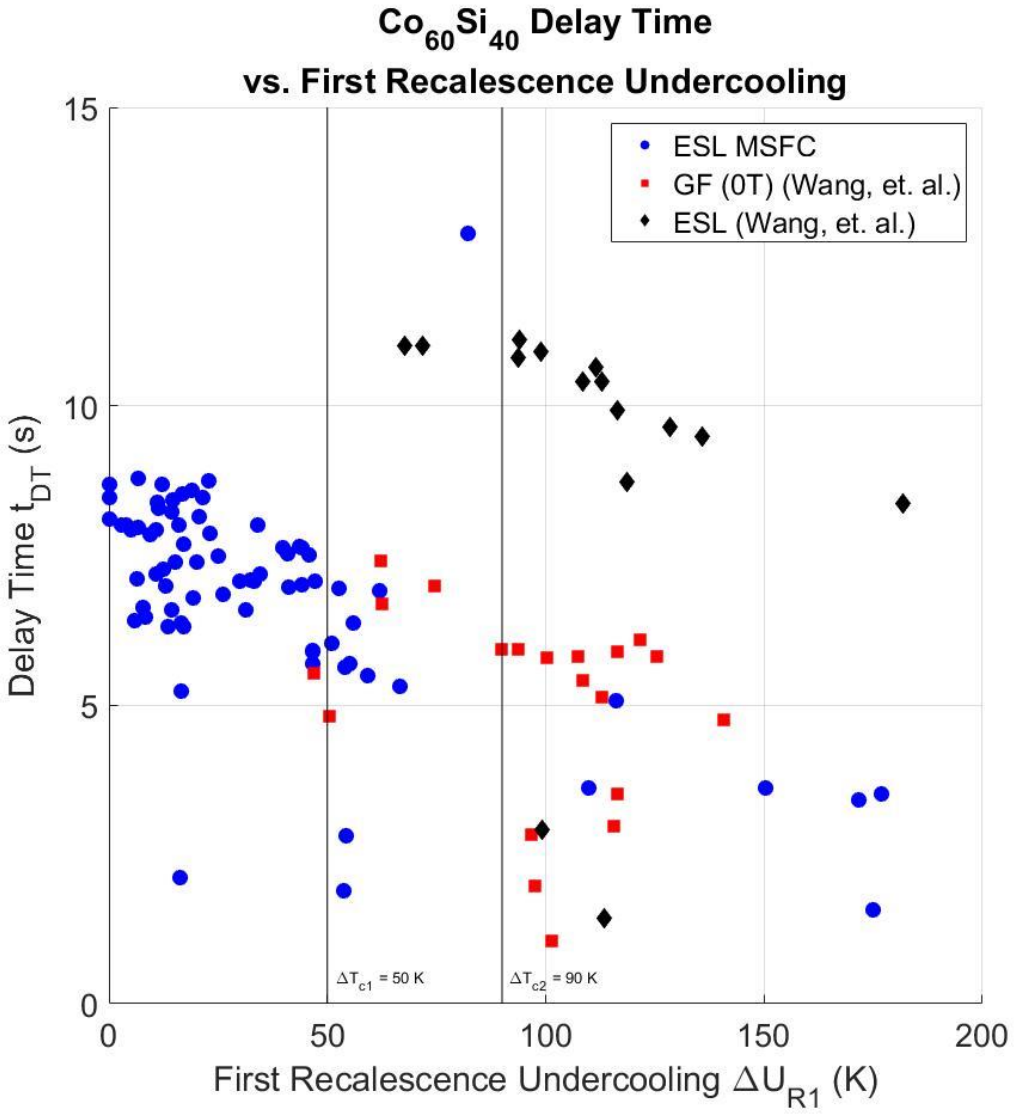

Figure 24: Delay time between recalescence events vs. the first recalescence undercooling for the $Co_{60}Si_{40}$ system

Several groupings are present when t_{DT} is graphed against ΔU_{R1}. Wang et. al. observed long delay times at high undercoolings in ESL testing, and postulated that the α-Co_2Si phase provided a difficult nucleant for CoSi. The lower delay times observed in the same split during the glass flux (GF) EML experiments are due to a higher melt convection present in EML that promotes fast nucleation. However, as EML data

covers the β-Co_2Si/CoSi phase split, it was concluded that the lower delay times for CoSi nucleation out of the α-Co_2Si phase were due to its ability to remelt easier than the β-Co_2Si phase [7]. Looking back at the ESL data covering this study and the Wang manuscript, it appears then that Co_2Si nucleates easier out of the primary CoSi phase than CoSi does out of either primary Co_2Si phase due to its lower delay time. However, the blue points gathered during this experiment seem to contradict the black ones in the primary α-Co_2Si phase split. It is difficult to distinguish between the β-Co_2Si and α-Co_2Si phases using results found from this experiment, as no metallography was done to directly identify structure formation, but it is clear that CoSi does not form primarily at temperatures greatly above ΔT_{c1}.

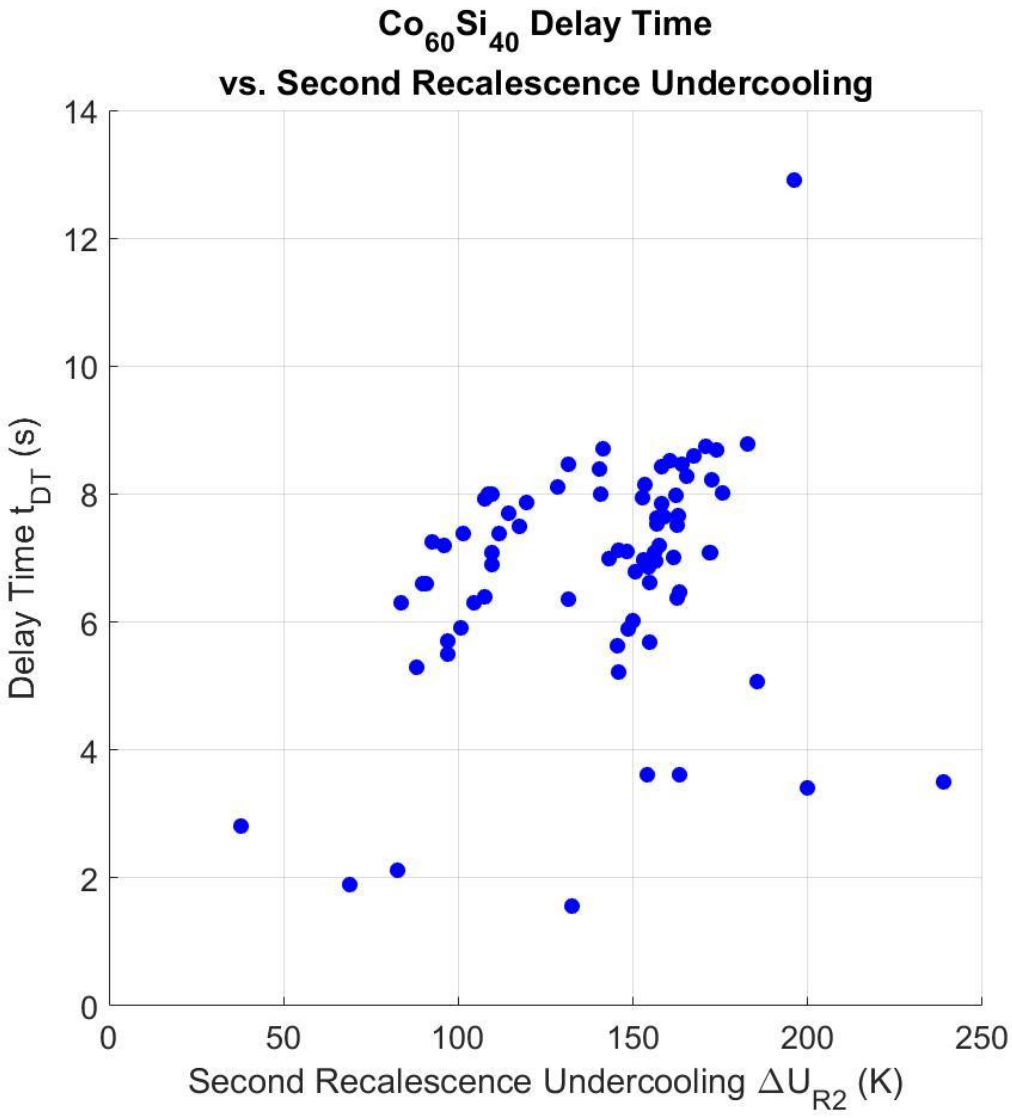

Figure 25: Delay time between recalescence events vs. the second recalescence undercooling for the $Co_{40}Si_{60}$ system

Due to a large number of samples with delay times between 5-9 seconds, the data presented in Figure 25 relating t_{DT} to ΔU_{R2} only shows one large grouping. It could be possible that a critical undercooling of $\Delta T_c \approx 120$ K could separate the group into two that each show increasing trends.

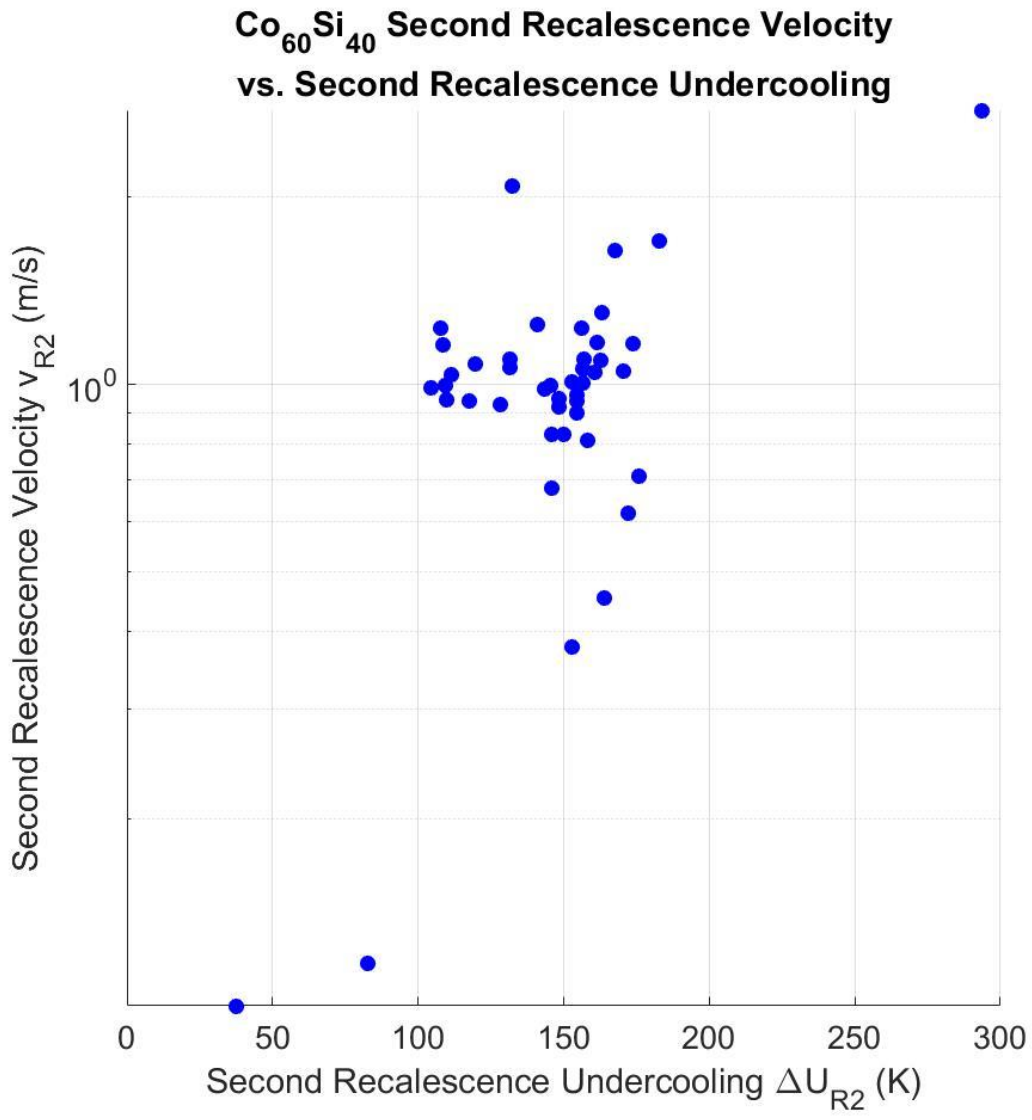

Figure 26: Second recalescence solidification velocity vs. the second recalescence undercooling for the $Co_{60}Si_{40}$ system

The grouping in Figure 26, where v_{R2} is graphed against ΔU_{R2} is again difficult to draw conclusions from. A lack of data points outside the central focus makes it hard to determine whether or not a critical undercooling is present. The lack of variant data in Figures 25-26 make it difficult to identify the secondary phases that form from the β-Co_2Si and α-Co_2Si phases.

6 Conclusions

Maximum temperature study

- The maximum temperature study was inconclusive, as no relationship was found between first recalescence high temperature and first recalescence undercooling for either sample. There was also no relationship between first recalescence high temperature and second recalescence undercooling.
- Maximum temperature during second recalescence was strongly correlated with undercooling during second recalescence, likely indicating the limits of the metastable extension to the equilibrium phase diagram.

Critical undercooling temperatures and regions defined

First recalescence

- For $Co_{38.5}Si_{61.5}$, there is a first recalescence critical undercooling of about 80 K that separates the system into multiple solidification pathways. This conclusion supports those of Yao [5], Zhang [3], and Li [8].
- For $Co_{60}Si_{40}$, there is a first recalescence critical undercooling of about 50 K that separates the system into multiple solidification pathways. This conclusion supports the work of Wang [7].

Second recalescence

- For $Co_{38.5}Si_{61.5}$, a second recalescence critical undercooling of 80 K appears necessary in order to decrease the energy barrier against nucleation to a level at which it can occur. This supports the theory that CoSi has difficulty nucleating out of the $CoSi_2$ phase [3] [8].

Metallography and delay times

- Results from preliminary metallography analysis show that a significant surface morphology change is associated with each delay time region for the $Co_{38.5}Si_{61.5}$ alloy.

Velocity

- First recalescence velocity is faster in the lower first recalescence undercooling region than in the higher region for $Co_{38.5}Si_{61.5}$. This is consistent with the suggestion that CoSi nucleates primarily at low undercoolings and $CoSi_2$ nucleates primarily at high undercoolings [7].
- Second recalescence velocity is faster in the higher first recalescence undercooling region than in the lower first recalescence undercooling region for both $Co_{38.5}Si_{61.5}$ and $Co_{40}Si_{60}$. This supports the conclusions that CoSi forms the secondary solid in these regions for both alloys [3] [7] [8].

7 Future Work

The temperature measurements found during the course of the experiment were taken by a pyrometer with a constant emissivity setting. Temperature values are accurate assuming the emissivity of the sample does not change during testing. However, as previously discussed, the sample emissivity often did change, resulting in incorrect temperature readings. It was found that the emissivity of the sample shifted during the second recalescence as a new phase formed. In the following melt cycle, the sample's emissivity reverted to its original value as it liquefied. These emissivity shifts resulted in spikes on the time-temperature graphs like the one observed in Figure 5 and were easily calibrated out to give accurate temperature data. The presence of emissivity shifts does raise an interesting potential for future experimentation, as understanding the exact emissivity value of each phase that forms could give insight into the solidification pathway of the material.

Investigating the microstructures of various samples tested using similar techniques as Wang [7] and Zhang [3] could provide additional insight into the structures formed during rapid solidification, as would further work involving the use of x-ray diffraction and spectrometry as discussed in reference [19]. Elemental analysis will also help identify phases present in metallographic images. In addition, similar experiments with the CoSi compounds studied are to be run using the EML facility on board the International Space Station (ISS) in order to better understand the solidification process under various stirring conditions.

8 References

[1] Materials Genome Initiative for Global Competitiveness, 2011.

[2] H.J. Fecht and R. Wunderlich, "Fundamentals of liquid processing in low earth orbit: from thermophysical properties to microstructure formation in metallic alloys", unpublished work.

[3] Y. K. Zhang, J. Gao, M. Kolbe, S. Klein, C. Yang, H. Yasuda, D. M. Herlach, and Ch.-A. Gandin, "Phase selection and microstructure formation in undercooled Co-61.8at.%Si melts under various containerless processing conditions", *Acta Materialia*, **61** (2013) 4861-4873.

[4] J. Lipton, W. Kurz, and R. Trivedi, "Rapid dendrite growth in undercooled alloys", *Acta Metallurgica*, **35** (1987) 957–964.

[5] W.J. Yao, N. Wang, and B. Wei, "Containerless rapid solidification of highly undercooled Co-Si eutectic alloys", *Materials Science and Engineering*, **A344** (2003) 10–19.

[6] Y. Inatomi, F. Onishi, and K. Kuribayashi, "Density and Thermal Conductivity Measurements for Silicon Melt by Electromagnetic Levitation under a Static Magnetic Field", *International Journal of Thermophysics*, **28** (2007) 44–59.

[7] Y. Wang, J. Gao, M. Kolbe, D. Holland-Moritz, A. Chuang, Y. Ren, and D. Matson, "In-situ studies of metastable solidification of undercooled Co60Si40 alloys using a high-speed camera and synchrotron radiation X-rays", unpublished work.

[8] M. Li, K. Nagashio, T. Ishikawa, A. Mizuno, M. Adachi, M. Watanabe, S. Yoda, K. Kuribayahi, and Y. Katayama, "Microstructure formation and in situ phase identification from undercooled Co–61.8 at.% Si melts solidified on an electromagnetic levitator and an electrostatic levitator", *Acta Materialia*, **56** (2008) 2514–2525.

[9] Q. Wang, L.-M. Wang, M.Z. Ma, S. Binder, T. Volkmann, D.M. Herlach, J.S. Wang, Q.G. Xue, Y.J. Tian, and R.P. Liu, "Diffusion-controlled crystal growth in deeply undercooled $Zr_{50}Cu_{50}$ melt on approaching the glass transition", *Physical Review B*, **83** (2011) 014202 1–5.

[10] J. Schroers, D. Holland-Moritz, D.M. Herlach, and K. Urban, "Growth kinetics of quasicrystalline and polytetrahedral phases of Al-Pd-Mn, Al-Co, and Al-Fe from the undercooled melt", *Physical Review B*, **61** (2000) 14 500–505.

[11] M. Li and K. Kuribayahi, "Nucleation-Controlled Microstructures and Anomalous Eutectic Formation in Undercooled Co-Sn and Ni-Si Eutectic Melts", *Metallurgical and Materials Transactions A*, **34A** (2003) 2999–3008.

[12] W.J. Yao, Z. Ye, H. Wang, X. Han, J. Wang, and X. Wen, "Competitive Nucleation and Rapid Growth of Co-Si Intermetallic Compounds during Eutectic Solidification under Containerless Processing Condition", *Journal of Materials Science and Technology*, **27** (2011) 1077–1082.

[13] M.N. Croker, D. Baragar, and R.W. Smith, "Anomalous eutectic growth", *Journal of Crystal Growth*, **30** (1975) 198–212.

[14] M. Trepczynska-Lent, "Rod and lamellar growth of eutectic", *Archives of Foundry Engineering*, **10** (2010) 179–184.

[15] X.X. Wei, X. Lin, W. Xu, Q.S. Huang, M. Ferry, J.F. Li, and Y.H. Zhou, "Remelting-induced anomalous eutectic formation during solidification of deeply undercooled eutectic alloy melts", *Acta Materialia*, **95** (2015) 44–56.

[16] S. Zhao, J. Li, L. Liu, and Y. Zhou, "Eutectic growth from cellular to dendritic form in the undercooled Ag–Cu eutectic alloy melt", *Journal of Crystal Growth*, **311** (2009) 1387–1391.

[17] S. Zhao, J. Li, L. Liu, and Y. Zhou, "Solidification of undercooled Ag–Cu eutectic alloy with the Sb addition", *Journal of Alloys and Compounds*, **478** (2009) 252–256.

[18] A.M. Mullis, C.R. Clopet, and R.F. Cochrane, "Determination of the origin of anomalous eutectic structures from in-situ observation of recalescence behavior", *Materials Science Forum*, **79** (2014) 349–354.

[19] O. Shuleshova, D. Holland-Moritz, W. Loser, A. Voss, H. Hartmann, U. Hecht, V. Witusiewicz, D.M. Herlach, and B. Buchner, "In situ observations of solidification processes in γ-TiAl alloys by synchrotron radiation", *Acta Materialia*, **58** (2010) 2408–2418.

[20] O. Shuleshova, unpublished work.

[21] D. Matson, "Pyrometer correction", 2016.

[22] S. Jeon, unpublished work.

[23] H. Yasuda, I. Ohnaka, Y. Mizutani, and Y. Waku, "Selection of eutectic systems in Al_2O_3-Y_2O_3 ceramics", *Science and Technology of Advanced Materials*, **2** (2001) 67-71.